Searching for SUSY in all hadronic final states with the α_T variable

Bryn Mathias
Imperial College London

Supervisor: Dr Alex Tapper

Abstract

This is a thesis.

Declaration

There are many like it.

Author

Preface

Something witty.

Acknowledgements

Thanks.

Contents

Chapter 1

Introduction

The accelerator and detectors The Large Hadron Collider (LHC) [6] is a proton-proton collider which is situated in the Large Electron Positron (LEP) tunnel approximately 100 m under the franco-swiss border. Design center of mass energy is 14 TeV with an instantaneous luminosity of $1 \times 10\text{e}^{34}\text{cm}^{-2}\text{s}^{-1}$. However during 2011 the center of mass energy was 7 TeV and the maximum luminosity was $5 \times 10\text{e}^{33}$ $\text{cm}^{-2}\text{s}^{-1}$. To achieve this high energy and high beam current the LHC uses superconducting niobium-titanium magnets, cooled to a temperature of 1.8 Kelvin, that produce a maximum field strength of 8.36 Tesla.

we might well need some more stuff about the LHC its self in here!

Situated around the LHC ring are four detectors, two general detectors ATLAS [4] and CMS (see Chapter 3 for a detailed discussion of the CMS detector) [18][25] which are designed to measure the Standard Model (S.M) to high precision and search for new physics. The LHC beauty experiment [20] is designed to study at previously unattainable precision the decays of heavy quark flavors, both to measure the S.M couplings and to search for beyond the S.M (BSM) physical processes. Finally the ALICE [5] experiment is designed to run when the LHC is running in it's secondary mode where rather than proton bunches, lead ions are collided, in an effort to study the quark-gluon plasma.

New physics Whilst the theory of the S.M and of new physics models will be discussed in chapter 2 it is prudent to discuss the observable features of these models with regard to design requirements for the general purpose detectors.

Chapter 2

Theory

2.1 The Constrained Minimal Super Symmetric Model

Chapter 3

The CMS detector

3.1 The High Level Trigger System

Chapter 4

Offline Object Reconstruction and Identification.

4.1 Hadronic Jets.

AK5 calo jets – explanation of the jet algos. How they are clustered at CMS. No need to mention PF? (we don't use it so why bother). Energy resolution, Jet energy corrections, ID. 2011 note

4.2 Electrons.

GSF elections - ID, use tracking. Veto on elections. 2011 note

4.3 Muons.

GPT muons - exact ID's, reconstruction methods. both veto and used to collect the control sample. 2011 note

4.4 Photons.

Chapter 5

Level One Calorimeter Trigger

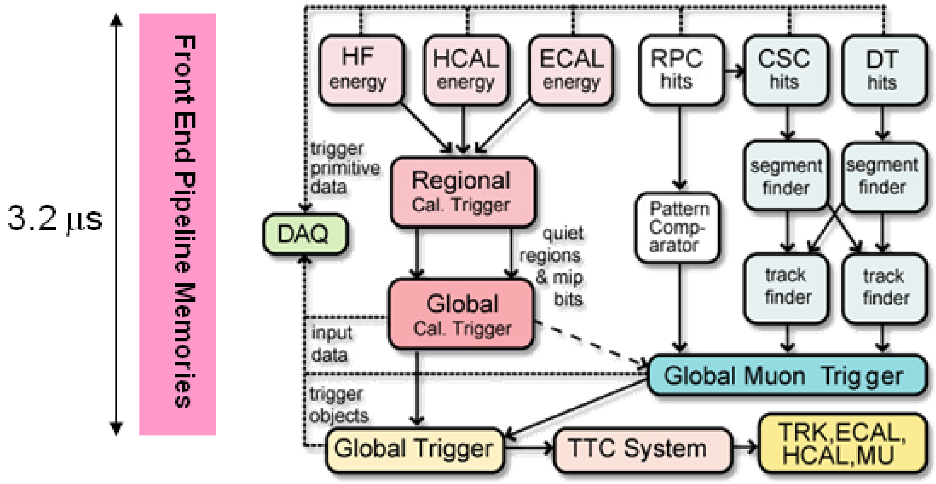

Figure 5.1: The CMS Level-1 Trigger system.

The CMS Level-1 trigger system[11] is a pipelined dead-timeless system based on custom-built electronics. The Level-1 trigger is a combination of several sub systems, which are interconnected as depicted in Figure 5.1.

Corse grain information from the electro-magnetic, hadronic and forward calorimeters is processed by the Regional Calorimeter Trigger (RCT), this is then passed to the Global Calorimeter Trigger (GCT) where the corse grain information is clustered in to physics objects, these objects are then passed to the Global Trigger where the Level-1 accept decision is made. Due to the limited size of the pipe line this Level-1 accept must be issued within 4.0 μs.

The objects passed from the GCT to the GT include electro-magnetic objects, both electrons and photons as due to the lack of tracking information at the Level-1 trigger these objects are indistinguishable, jets and energy sums.

The RCT generates up to 72 isolated and non-isolated electro-magnetic objects, these are sorted by rank, which is equivalent to transverse energy E_{T}. The four highest ranked electro-magnetic objects are then passed via the GCT to the GT at an equivalent data rate of 29 Gbs^{-1} per type.

Hadronic objects under go two clustering steps. First the transverse energy sums of the ECAL and corresponding HCAL towers are calculated, the towers are then summed in to 4×4 trigger regions, these are passed to the GCT at a data rate of 172.8 Gbs^{-1}. These trigger regions are clustered in to jet candidates by the GCT and ranked. The jets are then sub-divided in the categories depending on their pseudo-rapidity and the result of τ identification.

Energy sums come in two forms, the total transverse energy E_{T} which is the scalar sum of all transverse energies and the total jet transverse energy H_{T} which is calculated as the scalar sum of all jets above some programable threshold.

The missing energy equivalents of these $\not\!\!E_{\mathrm{T}}$ and $\not\!\!H_{\mathrm{T}}$ are formed from the negative vector sum of the objects considered for the transverse sums.

5.1 Level-1 Trigger Jet Algorithm [19]

The CMS detector can be un-rolled in the ϕ direction to form a rectangular grid of the 396 calorimeter regions, connected along the ϕ edge. The rectangle is formed from 18 ϕ divisions (from $-180° < \phi \leq 180°$) and 22 η divisions (from $-5 < \eta < 5$). Each ϕ division corresponds to 20°. The η divisions correspond to $\Delta\eta = 0.5$ in the forward calorimeters and to $\Delta\eta \approx 0.348$ in the barrel. A pictorial representation of this can be seen in figure 5.3.

A jet candidate is created if the sum of the ECAL and HCAL energies of the central calorimeter region has an energy deposit larger than all of its neighbours, as shown in figure 5.2 The jet is centred at this region where $p_T^{central} > p_T^{surrounding}$ and the transverse energies of the surrounding regions are summed in to the central region. The jet is then classified as a τ jet if $|\eta| < 3.0$ and none of the τ veto bits are set. If any τ vetoes are set the jet is classified as a central jet. The jet is classified as forward if $3.0 < |\eta| < 5.0$

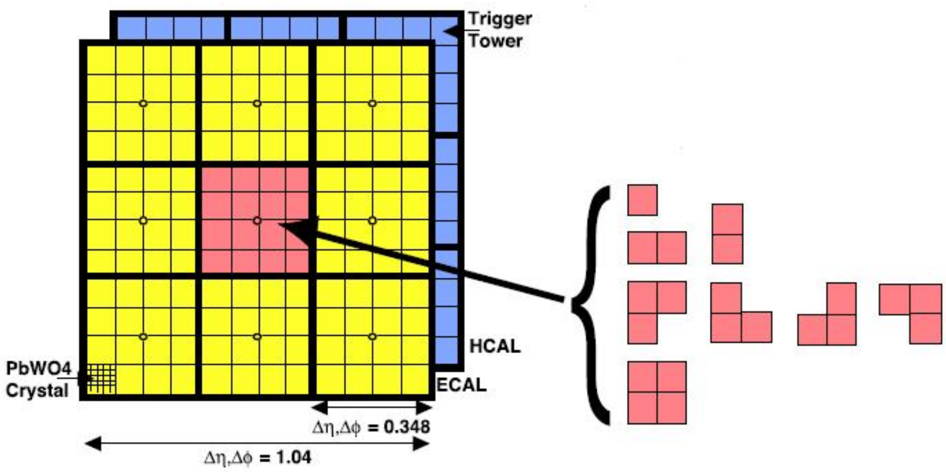

Figure 5.2: The 3×3 jet-finder window at Level-1. Each cell represents a trigger tower, which is the sum of the HCAL and ECAL transverse energies. The τ-jet veto patterns are shown to the right.

The τ-vetoes are set by the RCT depending on whether or not the energy depositions in up to four contiguous trigger towers are below a programmable fraction of the regional E_{T} as shown in Figure 5.2.

It is possible to apply separate jet energy corrections to each of the sub categories of GCT jets, however at current the same E_{T} and η dependant corrections are used for all three jet types.

In order to reduce the total data duplicated and shared between the jet finders the GCT employs a pre-clustering algorithm, which involves 18 jet finders operating simultaneously over the whole detector. These jet finders then only share information with neighbouring regions when the clustered jets are found. Figure 5.3 shows the boundaries between which the jet finders operate, these map naturally on to one RCT crate per jet finder. A maximum of 3 jets can be found on each of the ϕ strips acted on by the jet finders, this gives a maximum of 108 jets per event. In order to preserve continuity across the $\eta = 0$ boundary, the two adjacent trigger regions are shared between the jet finders.

An example of the jet finding is shown in Figure 5.4. The first step is to create a 2×3 mini cluster around any local maxima found in the 12×2 strip. Equality statements are imposed so that the energy of the central cell is greater than its neighbours in some directions and greater than or equal to the neighbours other directions to enforce a gap of at least one trigger region in both η and ϕ between the centres of the clustered jets.

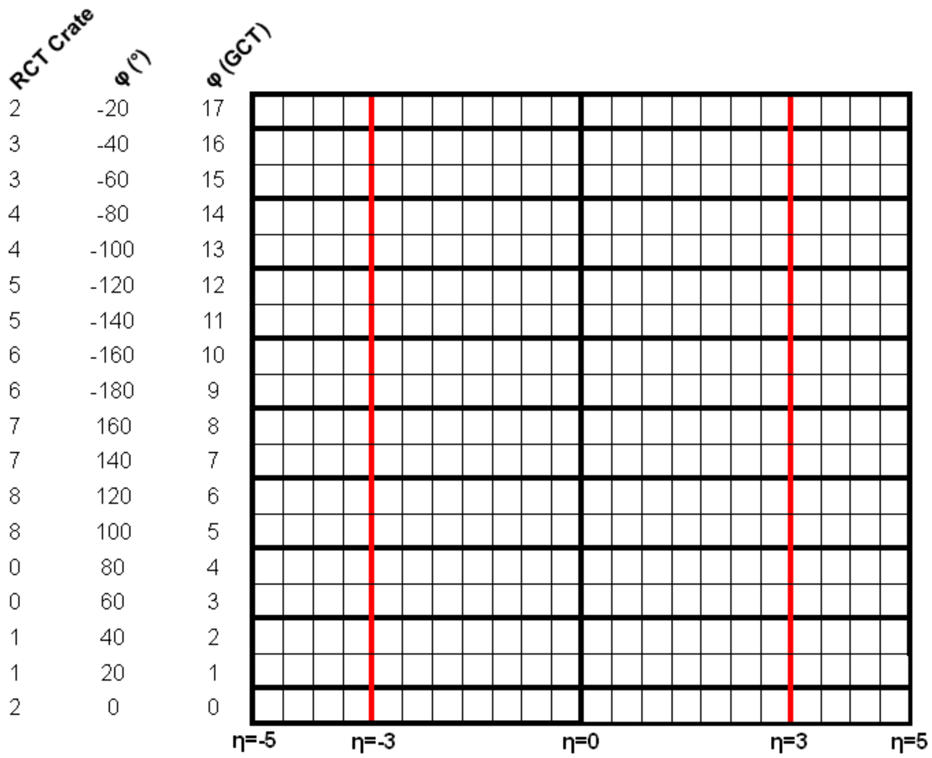

Figure 5.3: The calorimeter map that the 3×3 jet-finder operates over is made up for 396 calorimeter regions, each jet finder is mapped on to an RCT crate which is composed of an 11×2 strip of these regions. RCT crate labels are shown for negative η only.

In the second step the jet finder transfers the three largest mini clusters on a given ϕ strip to the closest ϕ strip on the neighbouring jet finder. These are then compared against the existing mini clusters in that ϕ strip, those that are adjacent or diagonally adjacent to a larger mini cluster are removed. The inequality statements are then reimposed to prevent problems with clusters having the same energies. In the final stages the mini clusters have their three adjacent regions summed in to produce a 3×3 jet cluster. Finally the four highest ranked jets are corrected and passed to the GT.

5.2 Level-1 Trigger Performance

During the start of data taking in 2010, no Jet Energy Corrections (JEC's) were applied in the Level-1 trigger. This gave a relatively slow turn on in therms of offline hadronic objects. During the winter shut down of the LHC between the 2010 and 2011 running periods a set of Level-1 JEC's were developed. These corrections used a peicewise cubic

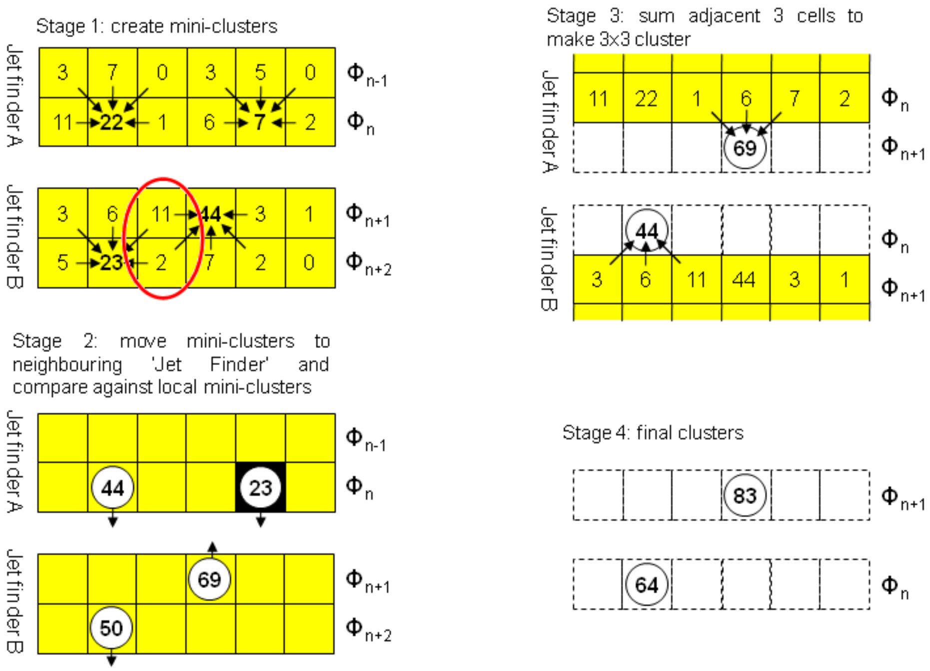

Figure 5.4: The Level-1 jet clustering method, six cells in η are shown. An example of overlapping jets is shown

form for the interpolation function used to correct the jet energy dependant on it's uncorrected E_{T} and η values. However as can be seen in Figure 5.5 these corrections were only applied to jets with a raw energy below 130 GeV, the secondary lobe shows those objects that do not have their energy corrected.

To overcome this a new set of corrections were derived using a well established tool for producing offline corrections,

REFERENCE TO tapper-001 here

using the same functional form that was derived for correcting particle flow jets.

REFERENCE TO PF HERE

In this section we discuss the performance of both sets of Level-1 JEC's and the performance of the energy sum triggers H_{T}, $\not\!\!H_{\mathrm{T}}$, and $\not\!\!E_{\mathrm{T}}$, the performance of which are not effected by the application of jet energy corrections at the Level-1 trigger due to the quantities being built from the internal GCT jets before they pass though the corrections look up table. The performance is studied under both low pile up conditions where the mean peak pile up $< PU >$ is 16 primary vertices and under high pile up conditions where $< PU >$ is 36 primary vertices.

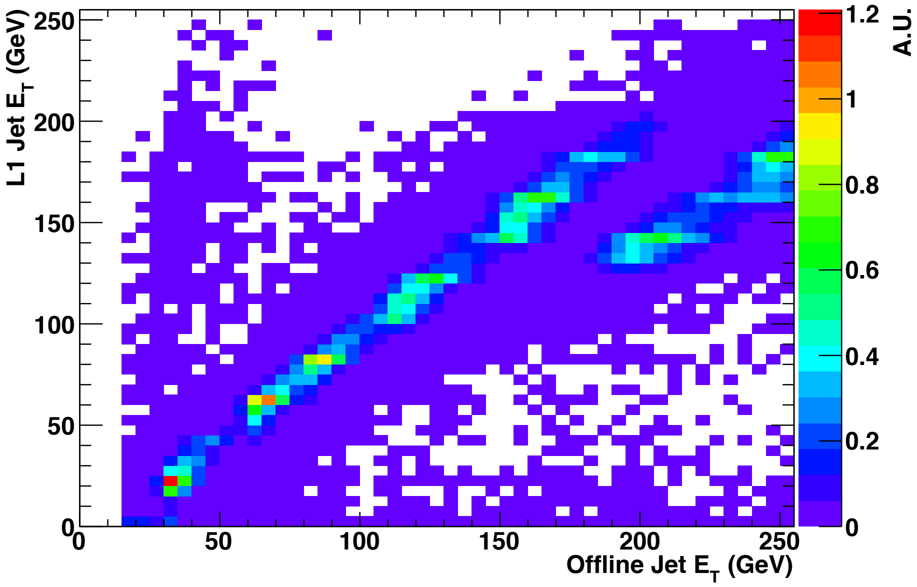

Figure 5.5: Correlation between offline corrected jet energy and Level-1 corrected jet energy for matched jets. The discontinuity shows where the Level-1 jet corrections do not alter the raw energy of the jet.

To measure the performance of the Level-1 single jet triggers we assume that the leading offline corrected anti-k$_t$(0.5) calorimeter jet is the jet that triggered the event. We then match this offline jet to the closest Level-1 jet in ΔR, where for there to be a match ΔR < 0.5 is required. For this match central, τ and forward jets are considered. Events where the recorded Level-1 energy is set to the overflow bit, meaning they have more than 254 GeV of E_{T} measured at Level-1 are ignored.

To collect an unbiased sample in which to measure the performance, two methods are used; the first is to require a Minimum Bias trigger, which is triggered by beam induced activity in the CMS detector. However due to the nature of these collisions the number of events with high energy interactions is low and the prescale applied to this trigger further reduces the sample size. However this method does produce the least bias. The second method is to trigger an object that does not deposit signifiant energy in the calorimeter systems, in this case we choose the muon trigger with the lowest un prescaled p_{T} threshold. The muon trigger is chosen with some loose isolation requirements to make sure it does not overlap with a jet, causing a discrepancy in the measure of the calorimetric energy. The sample has a higher number of events due to the large amount of bandwidth given to the single object muon triggers in CMS. The use of a muon trigger also serves to increase the precision of the measurement of the Level-1 missing energy trigger as the muons are not seen by the calorimeter system the $\not{E}_{\mathrm{T}}$ sample is enriched.

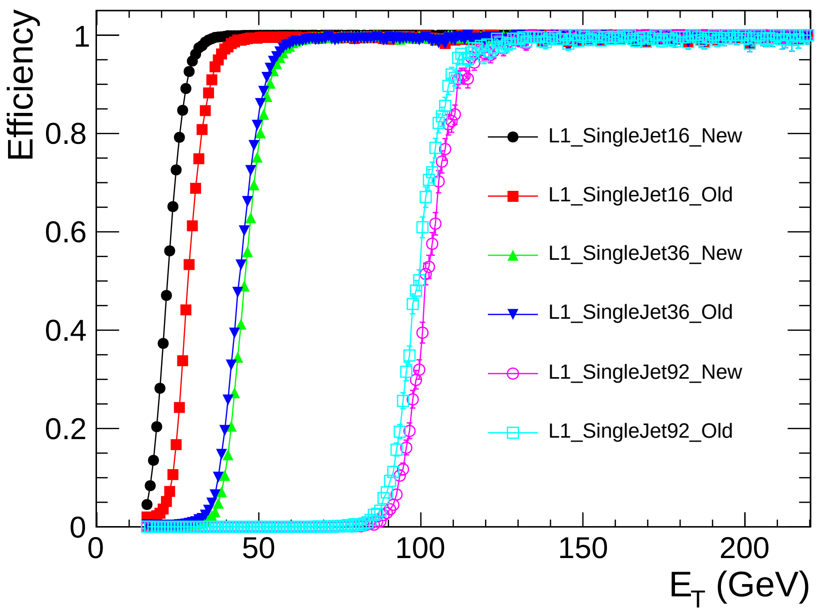

Figure 5.6: Comparison of the performance of L1_SingleJet16, L1_SingleJet36 and L1_SingleJet92, when using the piecewise cubic corrections and using the new correction scheme. The difference in performance of the two is negligible above 36GeV.

Figure 5.6 shows the performance of the piecewise cubic corrections (PWC) and the performance of the new corrections. The data was taken with the PWC enabled in the GCT hardware. The updated corrections were emulated in the bitwise reproduction of the GCT. The made an event by event comparison possible. At low E_{T} the new corrections turn on before the PWC corrections, if the new corrections were applied on with no change to the trigger menu, the Level-1 trigger rate would rise. At a threshold of 36 GeV and higher the performance of the two correction schemes is very similar. Due to the small change in observed performance and the ability to correct raw energies above 130 GeV, the new corrections were deployed online at the start of Run2011B and are still online at the end of data taking in 2012.

The performance of the updated corrections was then measured with data taken with the corrections applied in the GCT hardware. The reference sample was taken with the `HLT_IsoMu24_v*` high level muon trigger. The performance of three example triggers is show in Figure 5.7. The data collected and represented in Figure 5.7 has a peak mean pile up ($< PU >$) of 16 interactions, this is higher than the $< PU >$ of approximately 8-10

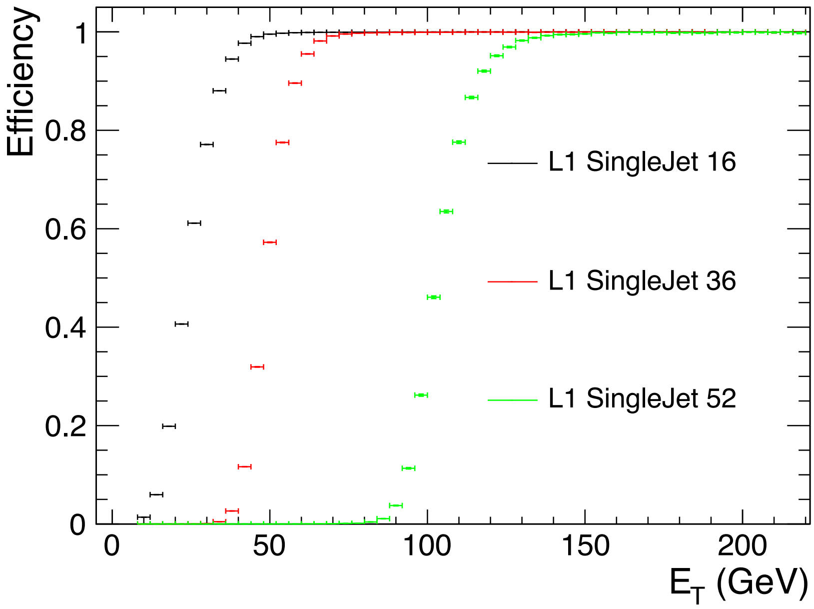

Figure 5.7: Performance measurements of L1_SingleJet16, L1_SingleJet36 and L1_SingleJet92, when using the new correction scheme deployed in the GCT hardware. The performance is slightly worse than that of the emulated triggers due to a change in pile up conditions between the two data taking periods.

present in Run2011A, on which the previous comparison was performed. The observed difference in the performance of the Level-1 single jet triggers as a function of pile up is a case of concern when data taking is underway at the LHC's design luminosity, where $< PU >$ is $>$36 at an instantaneous luminosity of $1{\times}10^{34} cm^{-27} s^{-1}$.

The instantaneous luminosity in 2012 was predicted to be $5{\times}10^{33} cm^{-27} s^{-1}$, with $< PU > \approx 32$. In order to study the effect on the trigger rate and efficiency a high pile up, low instantaneous luminosity, LHC fill was taken in 2011.

The Level-1 single jet performance was studied in this run in terms of two offline object definitions. The first was the standard anti-k$_t$(0.5) calorimeter jet reconstruction, the second was a set of anti-k$_t$(0.5) calorimeter jets which were corrected for pile up using the fastjet correction algorithm,

cite fast jet

which is further detailed in Section 4. The fast-jet corrections remove the energy deposited by the secondary interactions from the objects which are expected to come from the primary hard interaction, thus removing energy from the offline jets. The effect of these pile up corrections on the Level-1 trigger performance is first studied under conditions with $< PU >$ of 16, the performance of which has already been measured with respect to non pile up corrected offline objects, as a sanity check. The results are shown in Figure 5.8 , the performance is measured with respect to `HLT_IsoMu24_v*`, in terms of both pile up corrected and standard offline objects. As expected the performance in the two cases is very similar. The same comparison is shown for H_{T} in Figure 5.9, where the effect of the fastjet corrections is more pronounced due to the sum over jets. The difference between the turn on points for the two offline quantities is on the order of 10 GeV under low pile up conditions.

Due to the high pile up fill being a specialised fill with low instantaneous luminosity, the high level trigger paths were disabled, instead Level-1 trigger pass though paths were utilised to take the data. The Level-1 single muon pass though trigger is used to collect the reference sample. Otherwise the same analysis method is common between the two data sets. Figure 5.10 shows the difference in turn on for three example Level-1 single jet triggers when using standard calorimeter jets and fastjet corrected calorimeter jets. In the high pile up conditions the switch to offline jets that are corrected for pile up shifts the turn on point to lower vales of E_{T}, the magnitude of this effect reduces as the Level-1 trigger trigger threshold raises. This implies that the same offline performance as seen in the low pile up conditions can be achieved by using the pile up corrected offline objects and raising the Level-1 single jet trigger thresholds.

Figure 5.11 shows the same high pile up comparison, but for the Level-1 H_{T} triggers. Due to the size of the sample the precision of this measurement is low. However the same trend of a shift to lower H_{T} values of the turn on point of the Level-1 triggers when using pile up corrected offline objects is observed. This again implies that the Level-1 H_{T} trigger thresholds can be raised whilst preserving the same offline performance as during the low pile up conditions.

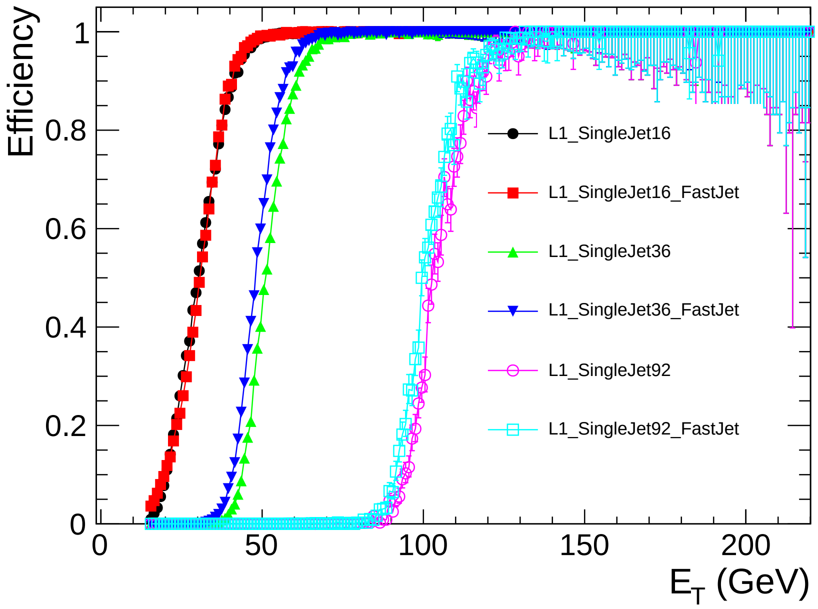

Figure 5.8: Comparison of the performance of L1_SingleJet16, L1_SingleJet36 and L1_SingleJet92 triggers. Where $< PU > = 16$. For two offline reconstruction methods, standard anti-k$_t$(0.5) calorimeter jets and pile up corrected anti-k$_t$(0.5) calorimeter jets.

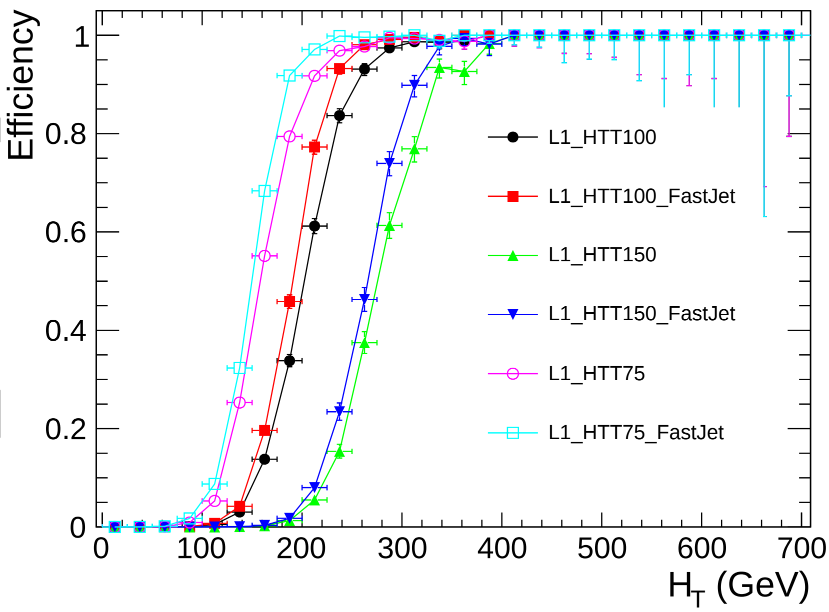

Figure 5.9: Comparison of the performance of L1_HTT75, L1_HTT100 and L1_HTT150 triggers. Where $< PU > = 16$. For two offline reconstruction methods, standard anti-k$_t$(0.5) calorimeter jets and pile up corrected anti-k$_t$(0.5) calorimeter jets.

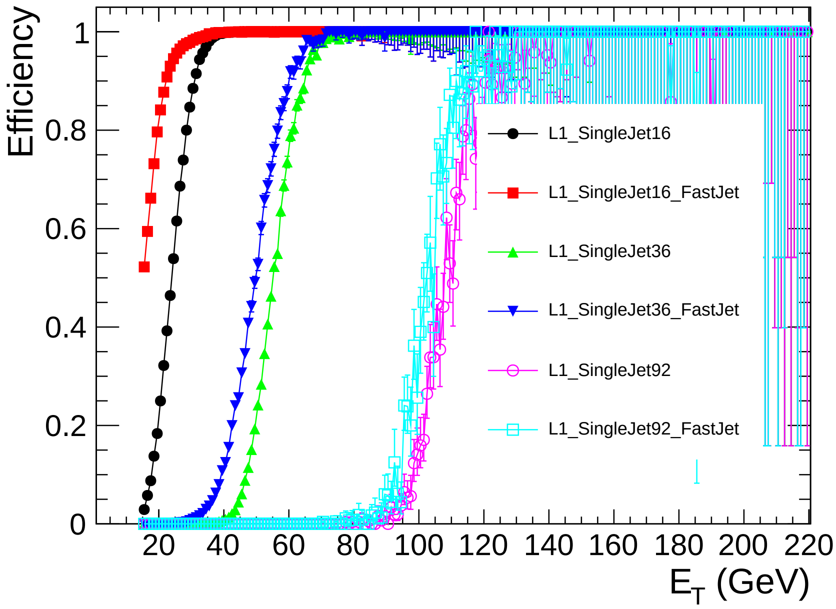

Figure 5.10: Comparison of the performance of L1_SingleJet16, L1_SingleJet36 and L1_SingleJet92 triggers. Where $< PU > = 36$. For two offline reconstruction methods, standard anti-k$_t$(0.5) calorimeter jets and pile up corrected anti-k$_t$(0.5) calorimeter jets.

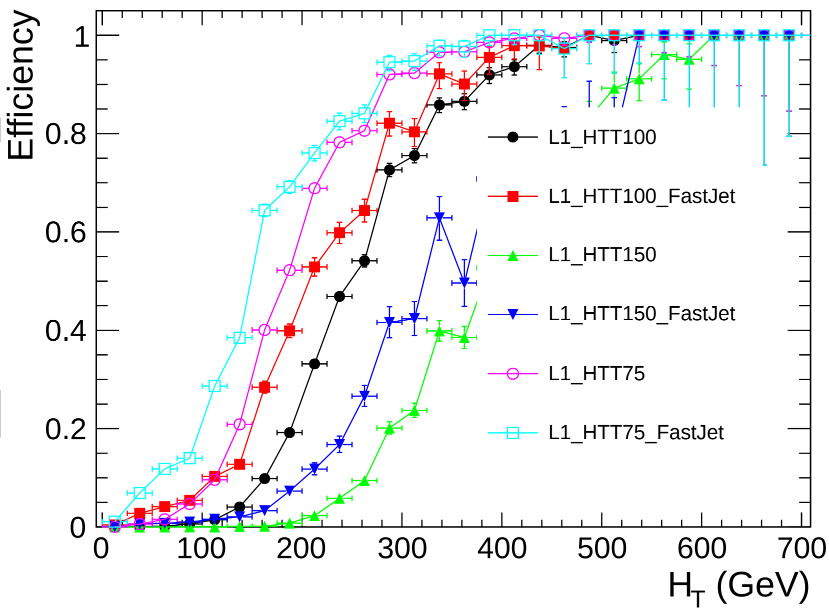

Figure 5.11: Comparison of the performance of L1_HTT75, L1_HTT100 and L1_HTT150 triggers. Where $< PU > = 36$. For two offline reconstruction methods, standard anti-k$_t$(0.5) calorimeter jets and pile up corrected anti-k$_t$(0.5) calorimeter jets.

5.3 Level-1 Trigger Pile-up Mitigation

Whilst we have seen that the offline performance of the Level-1 hadronic triggers can be maintained when raising the trigger thresholds to deal with increased rate, when switching to pile up corrected offline objects. Figure 5.14 shows the trigger cross section as a function of instantaneous luminosity for the `L1_HTT150` trigger, which requires $H_{\mathrm{T}} > 150$ GeV. However beyond a certain point raising thresholds causes a loss of performance. In this section we look at a method to reduce the effects of pile up hadronic Level-1 triggers, by making an addition to the Level-1 jet finding algorithm.

In Section 5.1 the Level-1 jet clustering algorithm was described. The proposed change was to add a requirement that the seeding region has a direct energy threshold, in addition to the equality relations that are set up. The effects of applying a 2 GeV or a 5 GeV threshold are studied. This threshold is on the raw, uncorrected energy of the trigger towers and effects all Level-1 jets. The impact will be seen in the Level-1 jet triggers which use corrected energy and Level-1 H_{T} and $\not{H}_{\mathrm{T}}$ which are formed from uncorrected jets. The aim is to remove the events which are accepted due to pile up, but not to remove physics events.

The triggers most effected by this change are the energy sum triggers as they sum many jets of low threshold, where as the single object triggers are already cutting on high E_{T} objects.

Figure 5.12(a) shows the internal GCT uncorrected jet energy spectrum in high pile up conditions, taken with the `L1_SingleMu` pass though triggers. The three histograms are for; no application of jet seed threshold in black, where there are many low E_{T} jets; In red a 2 GeV seed requirement is made, the effect is to cut out all jets below 2 GeV and cut out jets with an energy up to approximately 35 GeV of uncorrected energy; The blue histogram shows the jet energy spectrum after applying a 5 GeV seed threshold, the effect is to remove all jets below 5 GeV and to cut out jets with energy up to 55 GeV. Figure 5.12(b) shows the efficiency with respect to the no seed sample for the two test seed thresholds. The removal of jets in the low energy region of the E_{T} spectrum is where the advantage of applying a seed threshold is seen over simply raising the trigger thresholds, or raising the threshold of jets to be included in the Level-1 H_{T} or $\not{H}_{\mathrm{T}}$ calculation.

To quantify the effects of the addition of the jet seed a low pile up sample, where the effects are expected to be small, is studied in terms of rate reduction and efficiency change. The dedicated high pile up fill is then studied in terms of rate reduction, due to

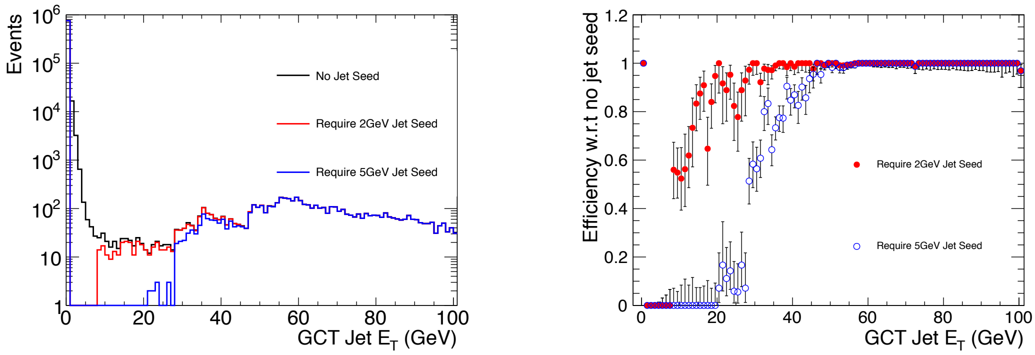

(a) GCT internal uncorrected jet E_{T} distributions for the same events with a 0, 2 or 5 GeV seed requirement.

(b) Efficiency of applying a requirement of 2 or 5 GeV with respect to no requirement.

Figure 5.12: Effect of requiring a jet seed threshold on GCT internal jets.

the limited sample size of the high pile up fill the change in efficiency on this sample is not studied. However due to the addition of energy from the secondary pile up interactions the change in efficiency in the low pile up sample is the worse case scenario.

Table 5.1 details the rate reduction with respect to the 0 GeV seed threshold for seed thresholds of 2 GeV and 5 GeV for three example triggers, these are:

- `L1_SingleJet50`, which requires at least one jet with $E_{\mathrm{T}} > 50$ GeV with in $|\eta| < 3.0$;
- `L1_QuadJet38`, which requires 4 jets with $E_{\mathrm{T}} > 38$ GeV with in $|\eta| < 3.0$;
- `L1_HTT100`, which requires that Level-1 $H_{\mathrm{T}} > 100$ GeV.

The rate of `L1_SingleJet50` is not effected by the requirement of a 2 GeV seed threshold and is reduced by 15% when a 5 GeV seed requirement is made. The `L1_QuadJet38` trigger rate is reduced by the same amount as the single jet trigger, under low pile up conditions for both seed thresholds. `L1_HTT100` sees a 2% rate reduction when requiring a 2 GeV seed threshold and a 3% reduction in rate when requiring a 5 GeV seed.

Table 5.2 shows the rate reduction under high pile up conditions with respect to the 0 GeV seed threshold requirement, for the same three example triggers as in the low pile up case. The rate of `L1_SingleJet50` is not reduced when making a 2 GeV seed requirement, when making a 5 GeV seed requirement the single jet 50 GeV rate is reduced by 30%. The rate of `L1_QuadJet38` is reduced by 30% when requiring a 2 GeV

Table 5.1: Summary of rate reduction during low pile up conditions.

Trigger	% rate reduction with a 2GeVrequirement	% rate reduction with a 5GeVrequiremen
L1_HTT100	$3 \pm 11\%$	$3 \pm 11\%$
L1_QuadJet38	$0 \pm 0\%$	$15 + 6 - 8\%$
L1_Jet50	$0 + 0 - 12\%$	$15 + 9 - 15\%$

Table 5.2: Summary of rate reduction during high pile up conditions.

Trigger	% of rate taken with 2GeVrequirement	% of rate taken with 5GeVrequirement
L1_HTT100	$40 \pm 5.7\%$	$99 + / - 50\%$
L1_QuadJet38	$30 \pm 20\%$	$40 + 22 - 24\%$
L1_Jet50	$0 + 7 - 0\%$	$30 + 10 - 12\%$

seed and by 40% when requiring a 5 GeV seed. The rate of `L1_HTT100` is reduced by 40% when requiring a 2 GeV seed threshold and when requiring a 5 GeV seed threshold the rate is reduced by $\approx 99\%$, however the statistical error on this prediction is large.

5.3.1 Effect on trigger efficiency

Section 5.3 shows that requiring a jet seed threshold substantially reduces the trigger acceptance rate at in high pile up conditions.

However the aim of requiring a jet seed is to reduce rate, but not at the cost of physics. In this section we look at the effects of requiring a seed threshold, whilst requiring some loose, generic offline selection on the hadronic objects.

The change in efficiency is measured under low pile up conditions where the least extra energy added to the event. This gives a worse case estimate of the effect of requiring a jet seed on the offline efficiency.

Each offline reconstructed calorimeter jet must adhere to the following quality criteria:

- Pass loose calorimeter ID;
- $p_{\mathrm{T}} \geq 30$ GeV;

- $|\eta| \leq 3.0$;
- Matched to a Level-1 jet with $\Delta R \leq 0.5$.

Where loose calorimeter ID is defined as; Electro-Magnetic fraction > 0.01, fraction of energy in the Hybrid Photo Diodes < 0.98 and the number of n90hits > 1.

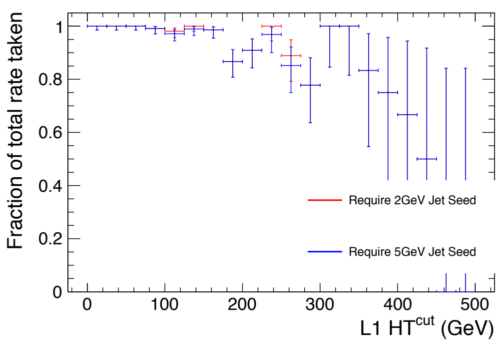

(a)

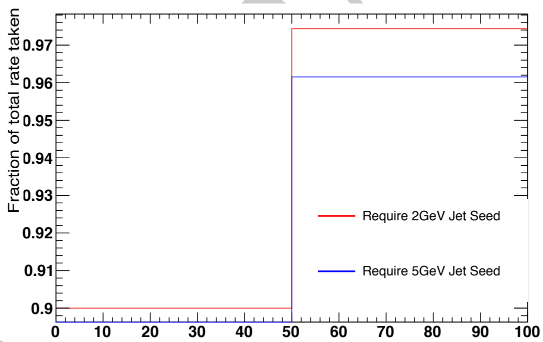

(b)

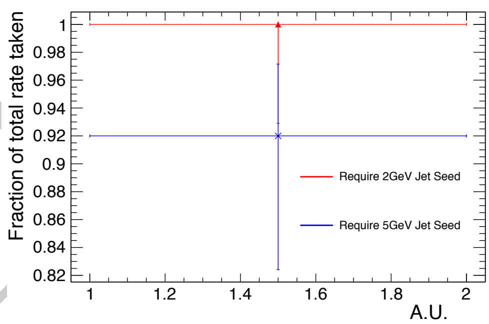

(c)

Figure 5.13: Efficiency reductions for various Level-1 algorithms when applying a 2 or 5 GeV seed tower requirement, in low pile up conditions. Figure (a) shows the efficiency reduction for H_T triggers at low pile up in cut steps of 25 GeV. Figure (b) shows the efficiency reduction for jets with in $|\eta| < 3.$ and $p_\mathrm{T} > 50$GeV. Figure (c) show the efficiency reduction for a quad jet trigger, with jet $|\eta| < 3.$ and $p_\mathrm{T} > 38$GeV.

Efficiency of H_T Triggers Figure 5.13(a) shows the acceptance reduction after applying the two jet seed thresholds. The distribution is the cumulative number of events passing a cut of $L1HT^{cut}$ in bins of 25 GeV. Due to H_T being the scalar sum of the jet p_T's in the event the value of Level-1 H_T is reduced as jets are removed from the calculation. To preserve efficiency the Level-1 trigger threshold will have to be reduced. When comparing to the high pile up rate reduction in table 5.2 it is shown that the trigger rate can be reduced by $\approx 20\%$ when requiring a 2 GeV seed threshold and reduced by $\geq 99\%$ when requiring a 5 GeV seed threshold, for a trigger threshold of 100 100 GeV.

Efficiency of Jet Triggers Figure 5.13(b) shows the change in acceptance of jets in low pile up conditions when the two seed thresholds are required. The effect is on the order of a few percent for each of the thresholds. Requiring a 2 GeV seed reduces the efficiency for jets above 50 GeV by $\approx 2.5\%$, whilst requiring a 5GeVseed reduces the efficiency of the same jets by $\approx 4\%$.

Efficiency of MultiJet Triggers Figure 5.13(c) shows that the effect of requiring a seed threshold of 2 GeV has no effect on the efficiency of the quad jet 38 GeV trigger and requiring a seed threshold of 5 GeV reduces the efficiency of the quad jet 38 trigger by 8%. The change in rate is dramatic in high pile up conditions where for a 2 GeV seed threshold the rate is reduced by $\approx 30\%$ and by $\approx 40\%$ when requiring a 5 GeV seed. However it is to be noted that the sample where this measurement has been made is of limited size, inferring a reasonably large statistical uncertainty.

5.3.2 Summary

The effects of requiring a jet seed have been studied using the Level-1 trigger emulator on high and low pile-up samples. The studies show that requiring a jet seed of 5GeVgreatly reduces the rate of the H_{T} and Multi Jet triggers in high pile up conditions, whilst not adversely effecting the data taking efficiency of these triggers.

The cross section of L1_HTT150 has been measured with and with out the addition of a jet seed threshold of 5 GeV as shown in Figure 5.14. Ideally the trigger cross section would be independent of the instantaneous luminosity and pile up, Figure 5.14 shows that the addition of a 5 GeV seed threshold reduces the dependance on instantaneous luminosity of the trigger cross section.

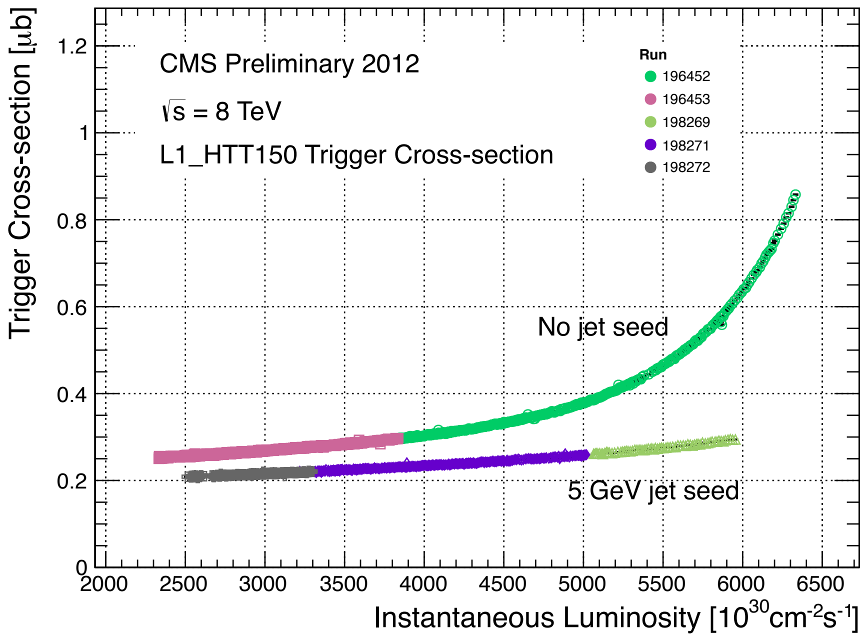

Figure 5.14: Trigger cross section as a function of number of pile up interactions. Showing that applying a 5 GeV jet seed threshold dramatically reduces the dependance of cross section on the instantaneous luminosity.

Chapter 6

The $\alpha_T$nalysis

Declaration In this chapter we discuss the main analysis performed as the subject of this thesis. For the theoretical motivations of this search please see Chapter 2. The analysis is based on the full 2011 data set which is made up of 5 fb^{-1} of 7 TeV data. However 5 fb^{-1} of the 2012 8 TeV is looked at to measure the performance of the upgraded α_T HLT paths.

6.1 The Problem

If Supersymmetry or some other beyond the S.M theory is to provide a yet undiscovered dark matter candidate, it is predicted that this candidate will interact via the weak nuclear force only. This gives a decay topology involving missing energy in the form of the dark matter particle escaping the detector. Due to the nature of interactions at the L.H.C, these particles would be produced at the end of a decay chain of heavy particles that interact strongly, giving a final topology involving hadronic objects which are classified as jets for the purpose of analysis and missing energy. There are several S.M processes that mimic this final state.

By far the largest of these backgrounds comes from QCD multi jet events where fake missing energy is introduced either from failures in reconstruction, or stochastic fluctuations in the calorimeter systems.

expand on this - E /sqrt E has non gaussian tails. Figures of jets falling below threshold, missed jets etc. probably from some jet-met paper.

However due to the theoretical errors on the QCD production cross section predicting the number QCD background events from Montecarlo simulation is not possible. A secondary QCD background also exists, where due to the requirement of a jet E_{T} threshold, multiple jets fall under threshold by a few GeV, this causes a balanced event to look unbalanced as the jets under threshold are no longer considered. It is these events that α_T is designed to remove.

The second major background comes from S.M electro-weak decays and is irreducible as the final states involve real missing energy, from neutrinos. The electro-weak decays that form the back ground are W $\rightarrow \tau\nu$ + Jets, where the τ is reconstructed as a jet, or the lepton fails the identification required for the dedicated lepton vetoes, Z $\rightarrow \nu\overline{\nu}$ + Jets is completely irreducible. These are generally di-jet topologies. At higher jet multiplicities top quark production followed by semi-leptonic top decay accounts of the largest background. These backgrounds are predicted using a well understood control sample this is fully explained in Section 6.6.

The final background source is that introduced by detector failure or electronic noise induced by the movement of the L.H.C proton beam. Approximately 1% of the ECAL read out is not available in offline event reconstruction, this provides a source of fake missing energy.

6.2 The α_T variable.

α_T is inspired by Ref [21] and was expanded to transverse multi jet topologies by members of the CMS collaboration in Refs [13, 14]. The purpose is to provide a variable that can be cut on to eliminate QCD from the final selection. To do this the inherent balance of the QCD system is exploited.

For di-jet systems α_T is defined as:

$$\alpha_T = \frac{E_T^{j_2}}{M_T} \tag{6.1}$$

where $E_T^{j_2}$ is the transverse energy of least energetic of the two jets and M$_T$ is defined as:

$$M_T = \sqrt{\left(\sum_{i=1}^{2} E_T^{j_i}\right)^2 - \left(\sum_{i=1}^{2} p_x^{j_i}\right)^2 - \left(\sum_{i=1}^{2} p_y^{j_i}\right)^2} \tag{6.2}$$

For a perfectly measured di-jet system with $E_T^{j_1} = E_T^{j_2}$, where the jets are opposite in ϕ $\alpha_T = 0.5$, for events with back to back jets where one is miss-measured $\alpha_T < 0.5$. However the majority of signals predict many jets in the final state. α_T can be generalised to work with n-jets in the flowing way. The variables H_{T}, $\not{H}_{\mathrm{T}}$ and ΔH_{T} are constructed:

$$H_{\mathrm{T}} = \sum_{i=0}^{n\ jets} E_T^{jet_i} \tag{6.3}$$

$$\not{H}_{\mathrm{T}} = \left|\sum_{i=0}^{n\ jets} \bar{p}_T^{jet_i}\right| \tag{6.4}$$

for jets above some predefined threshold E_{T} which is common for all jet based quantities. The multi jet system is reduced to a pseudo di-jet system by forming two large jets. The individual jet E_{T}'s are summed, with the final configuration being chosen to have the minimum difference in energy (ΔH_{T}) between the pseudo jets. This simple clustering criteria provides the best separation between miss-measured events and those with real $\not{E}_{\mathrm{T}}$.

α_T is then defined as:

$$\alpha_T = \frac{H_{\mathrm{T}} - \Delta H_{\mathrm{T}}}{2\sqrt{H_{\mathrm{T}}^2 - \not{H}_{\mathrm{T}}^2}} \tag{6.5}$$

Figure 6.1 shows the α_T distribution for both data and simulated background samples. The QCD multi jet background is negligible above an α_T value of 0.55, where as the standard model processes which involve real $\not{E}_{\mathrm{T}}$ exist at all possible values of α_T. Values of α_T in the range $0.5 < \alpha_T < 0.55$ arise in multi jet QCD due to jets falling below threshold or large stochastic fluctuations. It is to be noted that the discrepancy between data and simulation for $\alpha_T \leq 0.55$ is due to no trigger emulation being applied to the simulated background samples.

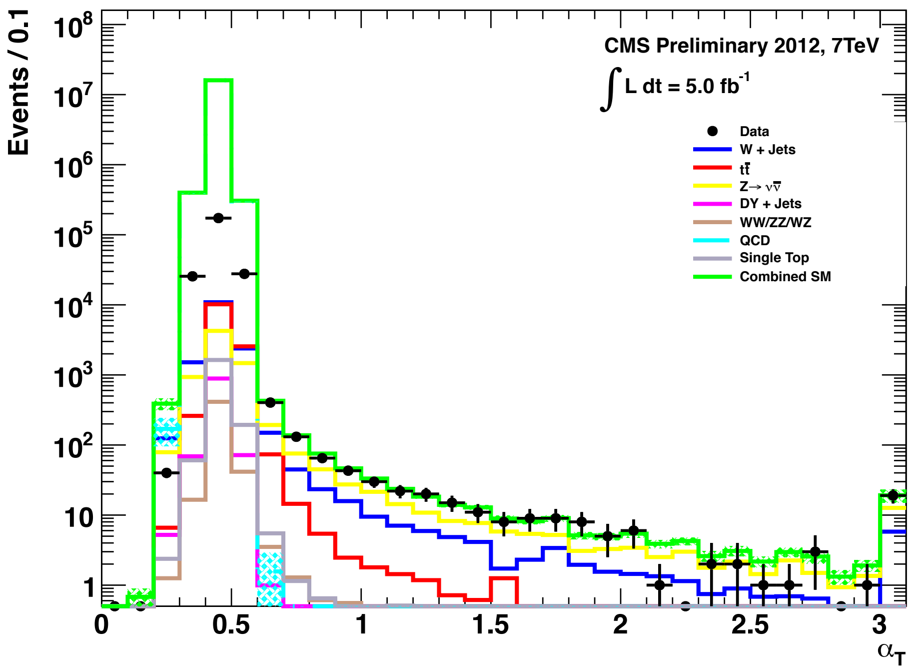

Figure 6.1: α_T distribution for background and data for the region $H_{\mathrm{T}} > 375$ GeV. Trigger emulation is not applied in the simulated background which leads to the discrepancy in the region $\alpha_T \leq 0.55$. The QCD multi-jet background is reduced to less than one event.

6.3 Event selection

In order to select events for the hadronic signal sample and the muon and photon control samples a common set of section cuts is defined. In this section the objects are defined as are the flow of the analysis cuts and filters.

Preselection of hadronic objects Jets are created by running the anti-k_t(0.5) jet clustering algorithm[9] over the calorimeter towers. More detail of the jet reconstruction at The Compact Muon Solenoid (C.M.S) is given in Section 4.1. The jets have their raw energies corrected based on their position and momentum to establish a uniform relative response in η and a calibrated absolute response in transverse energy E_{T}, with an associated uncertainty of between 2% and 4% dependant on E_{T} and η[10]. Jets considered in the analysis are required to have $E_{\mathrm{T}} > 50$ GeV, the highest E_{T} jet in the events is required to be within tracker acceptance ($|\eta| < 2.5$) and the sub leading jet is required to have $E_{\mathrm{T}} > 100$ GeV. In the lowest two offline H_{T} bins the jet thresholds are scaled to preserve the jet multiplicity, for the bin 275 GeV $< H_{\mathrm{T}}$ ¡ 325 GeV, the jet threshold is 36.$\dot{6}$ GeV and the sub leading jet threshold is 73.$\dot{3}$ GeV. In the bin 325 GeV $< H_{\mathrm{T}}$ ¡ 375 GeV, the jet threshold is 43.$\dot{3}$ GeV and the sub leading jet threshold is 86.$\dot{6}$ GeV.

The quantities H_{T} and $\not{H}_{\mathrm{T}}$ are then formed from these jets.

Elections Elections are reconstructed as described in Section 4.2. For the purpose of the analysis an object is defined as an electron if it has $p_{\mathrm{T}} > 10$ GeV, $|\eta| < 2.5$ and passes "VBTF" working point 95 quality criteria[15]. Any event containing an identified electron is vetoed.

Muons Muon reconstruction at C.M.S is detailed in Section 4.3. Signal events are vetoed if they contain a muon with $p_{\mathrm{T}} > 10$ GeV and $|\eta| < 2.5$ that passes the "VBTF" working point 95 for muons [17]. Two separate muon control samples are defined, one requiring exactly one muon with $p_{\mathrm{T}} > 10$ GeV, the second requiring two muons, who's invariant mass sums to the Z mass.

Photons Photon reconstruction as C.M.S is detailed in Section 4.4, signal events are vetoed if they contain a photon with $E_{\mathrm{T}} > 25$ GeV, $|\eta| < 2.5$ and that passes ID requirements[16]. A requirement of exactly one photon with $E_{\mathrm{T}} > 150$ GeV with in $|\eta|$ < 1.45 is made for the photon control sample.

PUT SOME STUFF IN ABOUT THE CROSS CLEANING

The use of these control samples will be discussed in Section 6.6.

The common selection cuts and filters consist of:

- **Good run selection**, All detector subsystems on, C.M.S in "Physics Declared" mode and all physics object groups have certified the runs and luminosity sections. This removes any events where the sub-detectors were in an error state or events from before the tracker was switched to high voltage mode.
- **P.K.A.M (Previously Known As Monsters) filter**, these events are caused by beam-gas interactions close to C.M.S, which cause a shower of particles to enter the pixel detector along the beam line, resulting in a large proportion of the pixel detector to record hits.

- **Vertex Selection** requires at least one non-fake vertex with at least four associated tracks, within a cylinder of radius 2 cm and length 48 cm, centred at Z = 0 of the C.M.S detector.

- **Hadronic barrel and end-cap noise filter**, this filter removes events where strips of towers in the hadronic calorimeters record energy from electrical noise, mimicking large, unbalanced energy deposits.

- **Vertex $p_\mathrm{T}/H_\mathrm{T} > 0.1$**, removes events where the sum of the p_T of all tracks from all good vertices is less than 10% of the energy deposited by jets in the calorimeters. This cut is designed to remove events with tracking failure, which would otherwise pass the calorimeter only event quality requirements.

- **Masked ECAL channel filter:** Approximately 1% of the ECAL crystals are masked, or have read out failure. To avoid selecting events with large energy miss measurement, a topological cut was devised. The first step is to calculate $\Delta\phi^*$ for each jet ($\vec{j}$) in the event, where:

$$\Delta\phi^* = \Delta\phi\left(\vec{\not{E}}_T + \vec{j}, \vec{j}\right). \tag{6.6}$$

  Which gives a measure of the miss measurement of a jet, if $\Delta\phi^*$ is small, the missing energy points along the jet in the ϕ direction. By selecting the miss measured jet, full position information is preserved. If any jet has $\Delta\phi^* < 0.5$, the number of masked ECAL crystals with in ΔR <0.3 are summed, if there are more than 10 masked crystals adjacent to the jet, the event is vetoed.

- **$R_{miss} < 1.25$:** The total hadronic energy in an event is required to be greater than 275 GeV which is well above the transverse energy threshold of 50 GeV for each jet. However several jets falling below this threshold can sum to a significant quantity of ignored energy. This is shown in Figure 6.2, here the missing energy calculated from jets in the range 10 GeV $< E_\mathrm{T} <$ 50 GeV is shown, whilst requiring that $\not{E}_\mathrm{T}$ $<$ 20 GeV. This shows that for a well balanced event the jets below threshold can carry greater than 100 GeV of ignored energy. R$_{miss}$ is defined as $\not{H}_\mathrm{T}/\not{E}_\mathrm{T}$ and can be used to single out events where the inclusion of lower momentum jets does significantly improve the balance of the event. Figure 6.3 shows for two H_T regions the R$_{miss}$ distribution after the application of the full cut flow, including α_T, QCD contamination is visible in the signal sample for R$_{miss} > 1.25$.

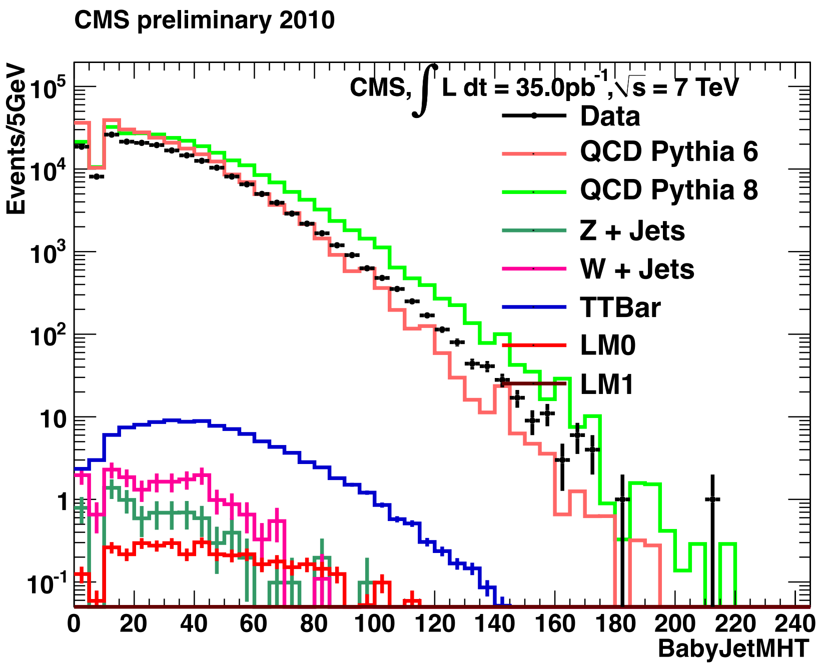

Figure 6.2: $\not\!\!H_{\mathrm{T}}$ from jets with 10 GeV $< E_{\mathrm{T}} <$ 50 GeV in events with $H_{\mathrm{T}} >$ 350 GeV and $\not\!\!E_{\mathrm{T}} <$ 20 GeV in 35 pb^{-1} of data.

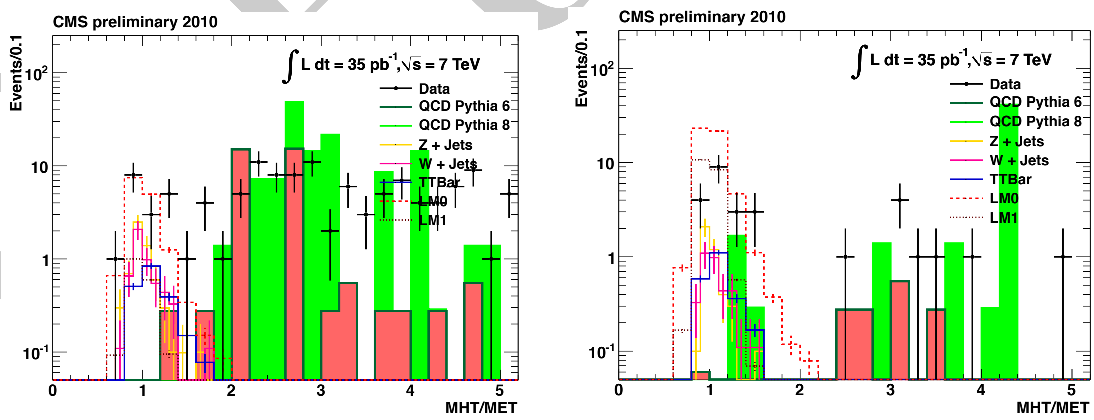

(a) (b)

Figure 6.3: (a) R$_{miss}$ distribution for events in the 250 GeV $<H_{\mathrm{T}}<$350 GeV region, where due to the low H_{T} requirement QCD contamination is enriched.
(b) R$_{miss}$ distribution for events in the $H_{\mathrm{T}}>$350 GeV region, QCD contamination occurs at R$_{miss} >$ 1.25.

This cut flow and set of object definitions define the common selection, on top of this an α_T cut is applied, the passing events are then binned in 8 H_T bins, these are 275 GeV - 325 GeV, 325 GeV - 375 GeV, 375 GeV - 475 GeV, 475 GeV - 575 GeV, 575 GeV - 675 GeV, 675 GeV - 775 GeV, 875 GeV - 7 TeV. However the raw number of events in the signal region is meaningless with out an accurate back ground prediction, as discussed earlier taking the background estimation from simulation is not viable due to the requirement of high order theory calculations on the cross sections of S.M processes involving jets, these have many divergencies due to the nature of QCD. Instead the simulation is used to form a translation factor between two samples measured in data, a control sample which closely mimics the S.M processes producing missing energy, but has a visible muon or photon in the final state. The background estimation methods are described and the background predictions stated in Section 6.6.

6.4 High Level triggers for the α_T nalysis

The CMS trigger system has been discussed in detail in Section 3.1 and Chapter 5, however details of analysis specific trigger paths were not discussed. During 2011 the first α_T specific trigger was designed and deployed online. The trigger was then upgraded for the higher luminosity and energy conditions of the 2012 data taking period.

The trigger takes advantage of cutting on two variables, H_T and α_T at low H_T a high α_T value cuts the trigger rate, where as at high H_T where the trigger rate is lower the α_T requirement can be loosened.

Due to the scaling of jet thresholds in the lowest offline H_T bins as detailed in Section 6.3 using a fixed jet threshold would cause inefficiency in the lowest offline H_T bins. To over come this the trigger level α_T calculation is performed iteratively for all jets above a predefined threshold. This raises the total number of accepted events whilst adding the benefit of being efficient for any offline jet threshold above the minimum trigger jet threshold.

Due to concerns on the time taken to perform the ΔH_T minimisation at the trigger and time constraints enforced on trigger menu development, the first implementation calculates α_T for the first 3 jets. For higher jet multiplicities the variable β_T is calculated.

$$\beta_T = \frac{H_\mathrm{T}}{2\sqrt{H_\mathrm{T}^2 - \not{H}_\mathrm{T}^2}} \tag{6.7}$$

this gives us the relation:

$$\alpha_T \leq \beta_T. \tag{6.8}$$

The decision flow is shown in Figure 6.4 and explained in detail below.

When a level one accept is issued the trigger bits that fired are checked, if the event fires a L1 muon trigger it is passed to the HLT muon triggers where only muon reconstruction is performed, reducing the reconstruction time. The α_T triggers are seeded on the lowest threshold unprescaled L1 H_T trigger, during 2011 this was L1_HTT100. Any events issuing a L1 accept and passing L1_HTT100 undergo calorimeter jet reconstruction, the reconstruction algorithm is detailed in Section 4.1.

Once the jets have been formed the trigger filter is entered. Initially the first two jets ranked by E_T, are considered, H_T and α_T are calculated, if both pass the trigger thresholds the event is accepted and the full detector read out is performed. If either H_T or α_T is below threshold, the next jet in E_T order is added, if the jet collection contains more than 3 jets then the β_T approximation is used. All jets in the event are added until either the even is accepted, or there are no more jets to be added above 40 GeV.

The effect of switching to the β_T approximation is to accept events that have missing energy due to miss-measurement, when calculating α_T offline these events have values of $\alpha_T < 0.5$. This introduces an impurity to the trigger and costs rate for events that will not be considered in the offline analysis.

6.4.1 Trigger efficiency measurement

The performance of the α_T trigger suit is measured with respect to a sample collected using the muon system. This allows the measurement of efficiency of both the level one seed trigger and the higher level trigger at the same time as different sub-systems are used to collect the reference and the signal triggers. This is due to the exclusive use of calorimeter jets in the α_T trigger, if more complicated reconstruction methods which produce an event hypothesis were used, muons would at HLT level only be considered as jets. Where as during calorimeter only reconstruction, muons are not considered and the p_{T} of any muons in an event is viewed as missing energy.

The selection for the trigger efficiency measurement is the same as listed in Section 6.3 with the requirement of exactly one well identified muon with $p_{\mathrm{T}} > 45$ GeV, the sum of the $\not{E}_{\mathrm{T}}$ in the event and the muon must add to the W mass and finally the muon must be separated by at least 0.5 in ΔR to the closest jet, to avoid the muon energy changing the energy of the jet offline when the cross cleaning is applied.

Due to the increase in luminosity over the running period the trigger thresholds were increased, to ensure constant rate though out the year and the trigger version numbers were increased each time the trigger menu was updated. The list of triggers considered and their reference triggers are listed in Tables 6.1 and 6.2.

The efficiency of each trigger version is measured in the required H_{T} bins, the total efficiency for each H_{T} bin is then calculated by combining the individual efficiencies using a weighted sum based on the fraction of the total luminosity of the sample that each version carries. This accounts for the change in running conditions during the data taking period and the criteria that the trigger suite takes constant rate over the length of then, the higher trigger versions and thresholds generally represent more integrated luminosity due to this.

The efficiency is measured as a function of the cumulative number of events, ie the efficiency at each point on the x axis is the measured efficiency if a cut were applied offline at that cut value.

As an example, the efficiency of each trigger used in the 275 GeV $< H_{\mathrm{T}} <$ 325 GeV bin is measured and then combined to give the total efficiency. The cumulative efficiency curves for each trigger seeding the lowest bin is show in Figures 6.5, 6.6 & 6.7. Note that some of the triggers are repeated, due to the reference trigger version incrementing and the signal trigger not.

These are then combined to give Figure 6.8 the efficiency at a cut of $\alpha_T > 0.55$ is 83.3% + 0.5% - 0.6%. The loss in efficiency comes from the disparity between the minimum thresholds for jets to enter the H_{T} and α_T calculations at the HLT and those used in the analysis. The trigger jet E_{T} threshold is 40 GeV where as the analysis jet E_{T} threshold in this bin is $36.\dot{6}$ GeV. The triggers used to take data at the end of this running period also have an α_T threshold above the analysis cut of $\alpha_T > 0.55$, which

Offline H_T bin	Signal Trigger	Reference Trigger
275 GeV $< H_\mathrm{T} <$ 325 GeV	HLT_HT250_AlphaT0p53_v2	HLT_Mu15_HT200_v2
275 GeV $< H_\mathrm{T} <$ 325 GeV	HLT_HT250_AlphaT0p53_v3	HLT_Mu15_HT200_v3
275 GeV $< H_\mathrm{T} <$ 325 GeV	HLT_HT250_AlphaT0p53_v4	HLT_Mu15_HT200_v4
275 GeV $< H_\mathrm{T} <$ 325 GeV	HLT_HT250_AlphaT0p53_v5	HLT_Mu30_HT200_v1
275 GeV $< H_\mathrm{T} <$ 325 GeV	HLT_HT250_AlphaT0p55_v1	HLT_Mu5_HT200_v4
275 GeV $< H_\mathrm{T} <$ 325 GeV	HLT_HT250_AlphaT0p55_v2	HLT_Mu40_HT200_v4
275 GeV $< H_\mathrm{T} <$ 325 GeV	HLT_HT250_AlphaT0p58_v3	HLT_DoubleMu8_Mass8_HT200_v4
275 GeV $< H_\mathrm{T} <$ 325 GeV	HLT_HT250_AlphaT0p58_v3	HLT_DoubleMu8_Mass8_HT200_v5
275 GeV $< H_\mathrm{T} <$ 325 GeV	HLT_HT250_AlphaT0p60_v3	HLT_DoubleMu8_Mass8_HT200_v4
275 GeV $< H_\mathrm{T} <$ 325 GeV	HLT_HT250_AlphaT0p60_v3	HLT_DoubleMu8_Mass8_HT200_v5
325 GeV $< H_\mathrm{T} <$ 375 GeV	HLT_HT300_AlphaT0p52_v1	HLT_Mu5_HT200_v4
325 GeV $< H_\mathrm{T} <$ 375 GeV	HLT_HT300_AlphaT0p52_v2	HLT_Mu8_HT200_v4
325 GeV $< H_\mathrm{T} <$ 375 GeV	HLT_HT300_AlphaT0p52_v3	HLT_Mu15_HT200_v2
325 GeV $< H_\mathrm{T} <$ 375 GeV	HLT_HT300_AlphaT0p53_v3	HLT_Mu15_HT200_v3
325 GeV $< H_\mathrm{T} <$ 375 GeV	HLT_HT300_AlphaT0p53_v4	HLT_Mu15_HT200_v4
325 GeV $< H_\mathrm{T} <$ 375 GeV	HLT_HT300_AlphaT0p53_v5	HLT_Mu30_HT200_v1
325 GeV $< H_\mathrm{T} <$ 375 GeV	HLT_HT300_AlphaT0p53_v6	HLT_Mu40_HT200_v3
325 GeV $< H_\mathrm{T} <$ 375 GeV	HLT_HT300_AlphaT0p53_v6	HLT_Mu40_HT200_v4
325 GeV $< H_\mathrm{T} <$ 375 GeV	HLT_HT300_AlphaT0p54_v5	HLT_Mu40_HT300_v4
325 GeV $< H_\mathrm{T} <$ 375 GeV	HLT_HT300_AlphaT0p54_v5	HLT_Mu40_HT300_v5
325 GeV $< H_\mathrm{T} <$ 375 GeV	HLT_HT300_AlphaT0p55_v3	HLT_DoubleMu8_Mass8_HT200_v4
325 GeV $< H_\mathrm{T} <$ 375 GeV	HLT_HT300_AlphaT0p55_v3	HLT_DoubleMu8_Mass8_HT200_v5

Table 6.1: List of α_T triggers used in the lowest two offline H_T bins and the triggers used to collect the reference sample.

Offline H_{T} bin	Signal Trigger	Reference Trigger
375 GeV $< H_{\mathrm{T}} <$ 475 GeV	HLT_HT350_AlphaT0p51_v1	HLT_Mu5_HT200_v4
375 GeV $< H_{\mathrm{T}} <$ 475 GeV	HLT_HT350_AlphaT0p51_v2	HLT_Mu8_HT200_v4
375 GeV $< H_{\mathrm{T}} <$ 475 GeV	HLT_HT350_AlphaT0p51_v3	HLT_Mu15_HT200_v2
375 GeV $< H_{\mathrm{T}} <$ 475 GeV	HLT_HT350_AlphaT0p51_v4	HLT_Mu15_HT200_v3
375 GeV $< H_{\mathrm{T}} <$ 475 GeV	HLT_HT350_AlphaT0p51_v5	HLT_Mu15_HT200_v4
375 GeV $< H_{\mathrm{T}} <$ 475 GeV	HLT_HT350_AlphaT0p52_v1	HLT_Mu30_HT200_v1
375 GeV $< H_{\mathrm{T}} <$ 475 GeV	HLT_HT350_AlphaT0p52_v2	HLT_Mu40_HT200_v3
375 GeV $< H_{\mathrm{T}} <$ 475 GeV	HLT_HT350_AlphaT0p52_v2	HLT_Mu40_HT200_v4
375 GeV $< H_{\mathrm{T}} <$ 475 GeV	HLT_HT350_AlphaT0p53_v10	HLT_Mu40_HT300_v4
375 GeV $< H_{\mathrm{T}} <$ 475 GeV	HLT_HT350_AlphaT0p53_v10	HLT_Mu40_HT300_v5
475 GeV $< H_{\mathrm{T}} <$ 7 TeV	HLT_HT400_AlphaT0p51_v1	HLT_Mu5_HT200_v4
475 GeV $< H_{\mathrm{T}} <$ 7 TeV	HLT_HT400_AlphaT0p51_v2	HLT_Mu8_HT200_v4
475 GeV $< H_{\mathrm{T}} <$ 7 TeV	HLT_HT400_AlphaT0p51_v3	HLT_Mu15_HT200_v2
475 GeV $< H_{\mathrm{T}} <$ 7 TeV	HLT_HT400_AlphaT0p51_v4	HLT_Mu15_HT200_v3
475 GeV $< H_{\mathrm{T}} <$ 7 TeV	HLT_HT400_AlphaT0p51_v5	HLT_Mu15_HT200_v4
475 GeV $< H_{\mathrm{T}} <$ 7 TeV	HLT_HT400_AlphaT0p51_v6	HLT_Mu30_HT200_v1
475 GeV $< H_{\mathrm{T}} <$ 7 TeV	HLT_HT400_AlphaT0p51_v7	HLT_Mu40_HT200_v3
475 GeV $< H_{\mathrm{T}} <$ 7 TeV	HLT_HT400_AlphaT0p51_v7	HLT_Mu40_HT200_v4
475 GeV $< H_{\mathrm{T}} <$ 7 TeV	HLT_HT400_AlphaT0p51_v10	HLT_Mu40_HT300_v4
475 GeV $< H_{\mathrm{T}} <$ 7 TeV	HLT_HT400_AlphaT0p51_v10	HLT_Mu40_HT300_v5
475 GeV $< H_{\mathrm{T}} <$ 7 TeV	HLT_HT400_AlphaT0p52_v5	HLT_Mu40_HT300_v4
475 GeV $< H_{\mathrm{T}} <$ 7 TeV	HLT_HT400_AlphaT0p52_v5	HLT_Mu40_HT300_v5

Table 6.2: List of α_T triggers used in the $H_{\mathrm{T}} > 375$ GeV bins and the triggers used to collect the reference sample.

H_{T} range (GeV)	Trigger efficiency (%)
275–325	$83.3^{+0.5}_{-0.6}$
325–375	$95.9^{+0.7}_{-0.9}$
375–475	$98.5^{+0.5}_{-0.9}$
475–∞	$100.0^{+0.0}_{-4.8}$

Table 6.3: Efficiencies of the α_T triggers used in the 7 TeV α_T analysis on 5 fb^{-1} of LHC data.

again causes an inefficiency. The list of efficiencies for each H_{T} bin are shown in Table 6.3. The trigger efficiencies are measured to better than one percent and this information is used in the final likelihood model, to correct the expected numbers from simulation when calculating the translation factors.

The α_T triggers were upgraded for the increased instantaneous luminosity and pile up conditions expected during the 2012 data taking period. The first stage was to implement the full α_T calculation for each addition of a new jet, this change increases the purity of the trigger, meaning that for the same threshold the rate taken is lower than that of the previous algorithm. This allows the thresholds to be kept low, whilst not increasing the overall trigger rate.

The second upgrade was to switch to pile up corrected jets at the HLT, this change keeps the trigger cross section liner as a function of instantaneous luminosity.

The third choice was to design a trigger suite that could run for the entire 2012 data taking period, with out changing the trigger thresholds, this was done to make the measurement of the efficiency simpler.

The trigger thresholds used are presented in Table 6.4, due to the constant thresholds in H_{T} and α_T though out the run, the versioning of the triggers is excluded from this table. The efficiency of the triggers is measured for 11.7 fb^{-1} of LHC data taken at a centre of mass energy of 8 TeV the efficiencies were measured for the analysis presented at HCP, documented in [3]. A single muon trigger is used to collect the reference sample, the threshold of this trigger was unchanged during the data taking period, the path selected is `HLT_IsoMu24_v*` which requires at least one muon with $p_{\mathrm{T}} > 24$ GeV that is not over lapping with any other object in the detector. The same method is used as for

H_{T} range	Trigger
275 GeV–325 GeV	HLT_HT250_AlphaT0p55_v*
325 GeV–375 GeV	HLT_HT300_AlphaT0p53_v*
375 GeV–475 GeV	HLT_HT350_AlphaT0p52_v*
475 GeV–8 TeV	HLT_HT400_AlphaT0p51_v*

Table 6.4: Triggers used to seed the analysis H_{T} bins during 2012 data taking.

H_{T} range (GeV)	Trigger efficiency (%)
275 GeV – 325 GeV	$89.6^{+0.4}_{-0.4}$
325 GeV – 375 GeV	$98.6^{+0.2}_{-0.3}$
375 GeV – 475 GeV	$99.4^{+0.2}_{-0.3}$
475 GeV – 8 TeV	$100.0^{+0.0}_{-0.5}$

Table 6.5: Efficiencies of the α_T triggers at a centre of mass energy of 8 TeV α_T measured in 11.7 fb^{-1} of LHC data.

the 2011 trigger efficiency measurement. However the offline jets are corrected for pile up using the fast jet corrections, to stay inline with the HLT object definitions.

Figure 6.9 shows the efficiencies of the four individual triggers that seed the 275 GeV–325 GeV H_{T} bin for 11.7 fb^{-1} of 8 TeV LHC data, Figure 6.10 shows the combined cumulative efficiency of the 2012 trigger suite.

The two trigger suites have very similar offline performance with 100% efficiency in the analysis bins above 475 GeV and high efficiency in the lower bins. To quantify the difference in performance between the two algorithms the purity is defined as the number of events passing the trigger that pass the offline α_T requirement at the same threshold as the trigger requirement divided by the total number of events accepted by the trigger. The purity of each trigger algorithm is measured for an example trigger with a H_{T} threshold of 350 GeV and an α_T threshold of 0.52. The 2011 trigger which only performs the full α_T calculation for jet multiplicities of less than four has a purity of 48%, which means a quarter of all rate taken by the trigger is used in the offline analysis. The 2012 trigger which performs the full α_T calculation for all jet multiplicities has a purity of 75%. This 25% increase in purity translates in to a 25% rate reduction for the same trigger threshold when changing to the full α_T calculation for all jet multiplicities, thus enabling the trigger thresholds to be kept at the same or lower thresholds in the 2012 run as in the 2011 run.

6.5 Extension to higher analysis dimensions.

Whilst it should be noted that the author did not contribute towards the extension of the analysis to include a dimension based on the measurement of the number of jets containing b quarks in the final state, the final analysis does include this extension, hence the b-tagging procedure is explained in sufficient detail as to understand the process but not to elude to all the nuances of the method in the following section.

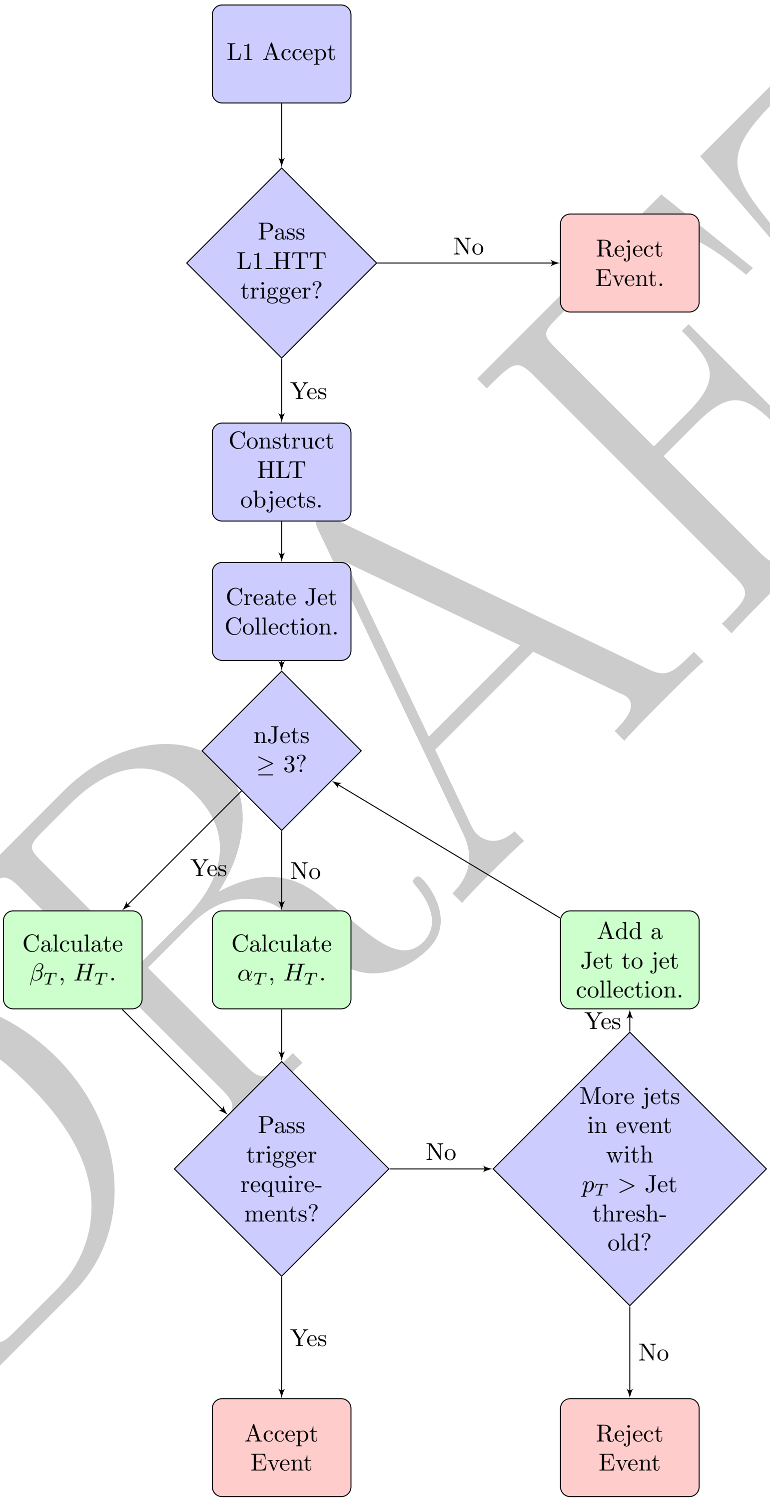

Figure 6.4: Flow chart representing the steps taken to make a trigger decision using the α_T trigger algorithm.

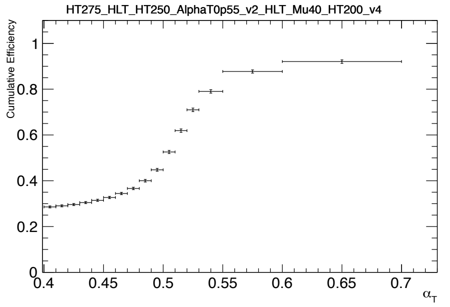

(a) HLT_HT250_AlphaT0p55_v1

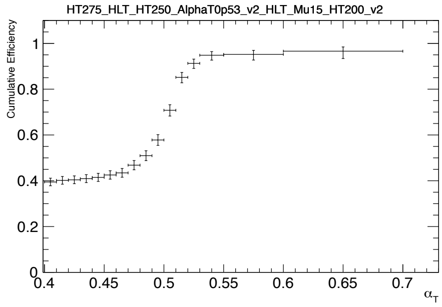

(b) HLT_HT250_AlphaT0p53_v2

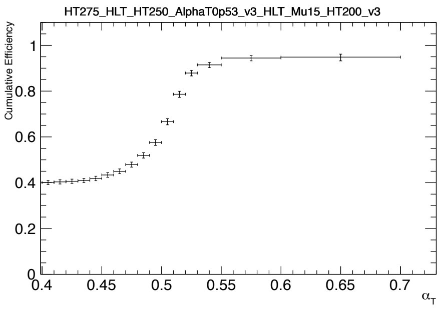

(c) HLT_HT250_AlphaT0p53_v3

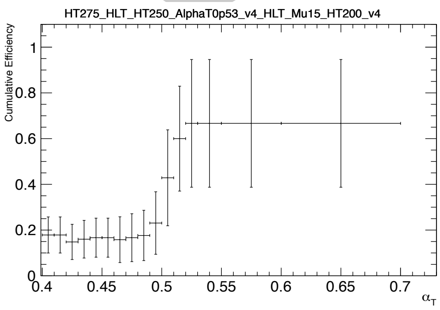

(d) HLT_HT250_AlphaT0p53_v4

Figure 6.5: Turn on curves for the individual α_T triggers used to seed the 275 GeV $< H_{\mathrm{T}} <$ 325 GeV bin.

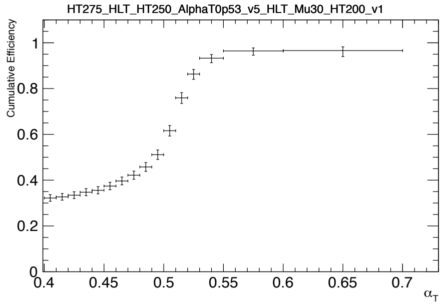

(a) HLT_HT250_AlphaT0p53_v5

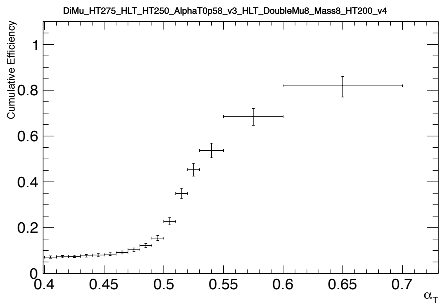

(b) HLT_HT250_AlphaT0p58_v3

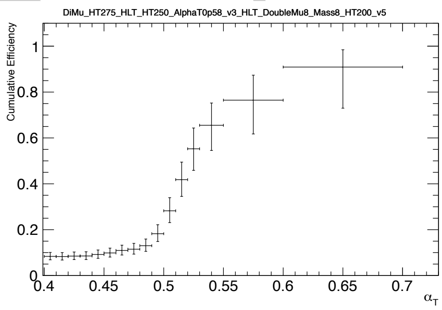

(c) HLT_HT250_AlphaT0p58_v3

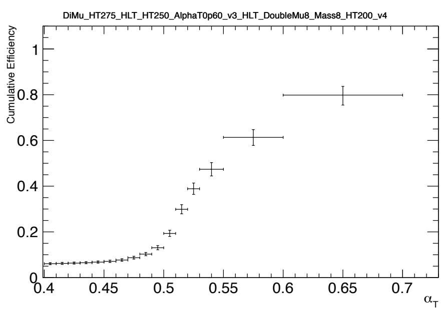

(d) HLT_HT250_AlphaT0p60_v3

Figure 6.6: Turn on curves for the individual α_T triggers used to seed the 275 GeV $< H_{\mathrm{T}} <$ 325 GeV bin.

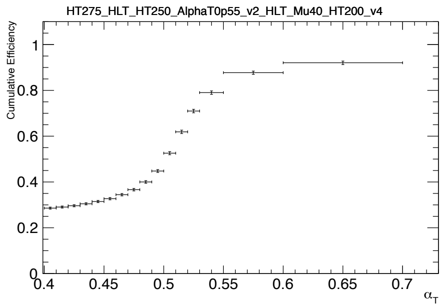

(a) HLT_HT250_AlphaT0p60_v3

Figure 6.7: Turn on curves for the individual α_T triggers used to seed the 275 GeV $< H_{\mathrm{T}} <$ 325 GeV bin.

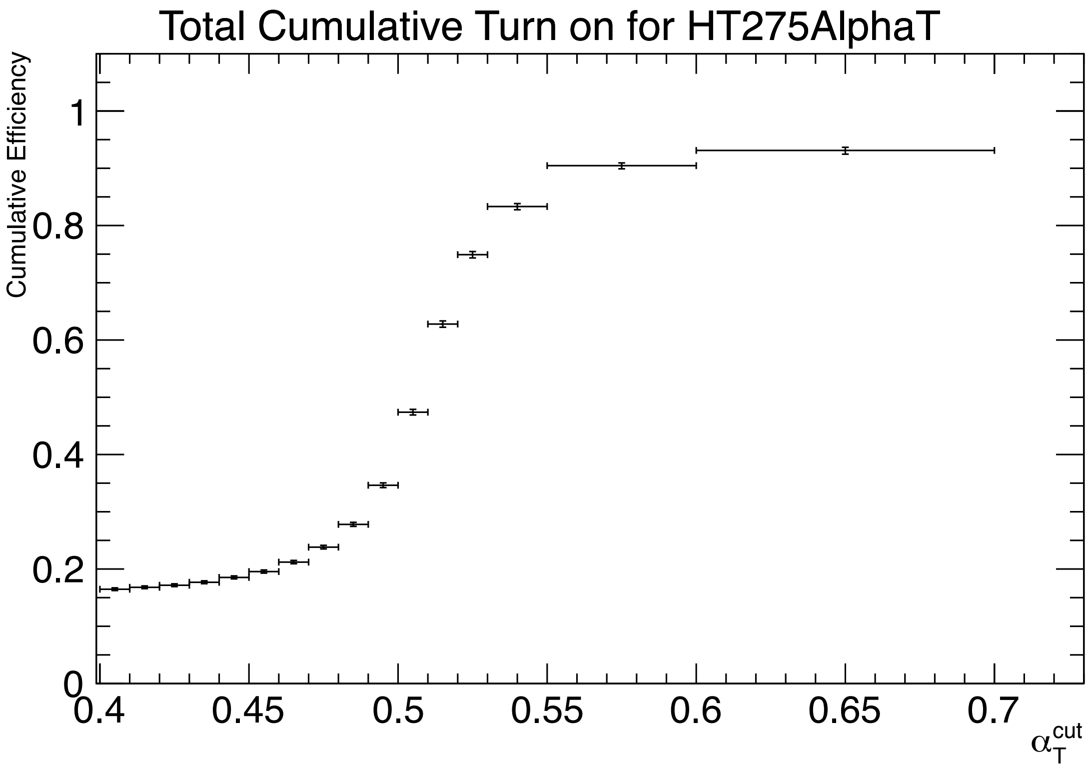

Figure 6.8: Combined cumulative efficiency for the triggers seeding the 275 GeV $< H_{\mathrm{T}} <$ 325 GeV offline analysis bin.

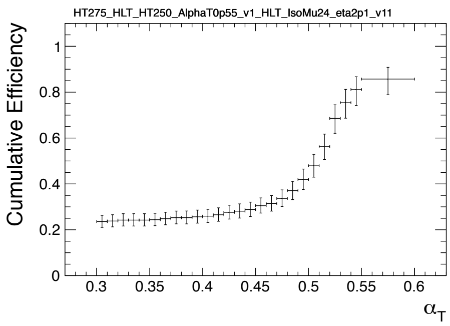

(a) HLT_HT250_AlphaT0p55_v1

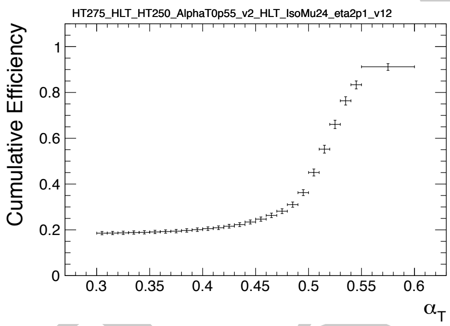

(b) HLT_HT250_AlphaT0p55_v2

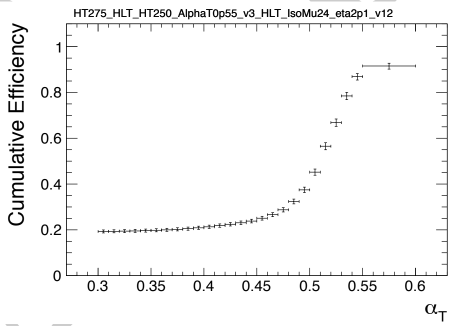

(c) HLT_HT250_AlphaT0p55_v3

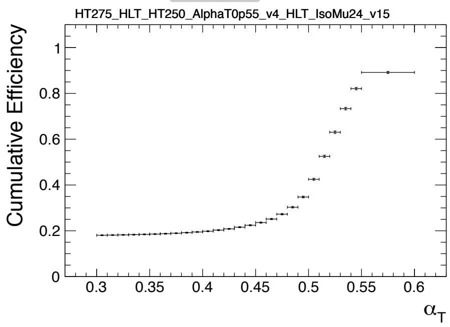

(d) HLT_HT250_AlphaT0p55_v4

Figure 6.9: Turn on curves for the individual α_T triggers used to seed the 275 GeV $< H_{\mathrm{T}} <$ 325 GeV bin, during 2012 data taking.

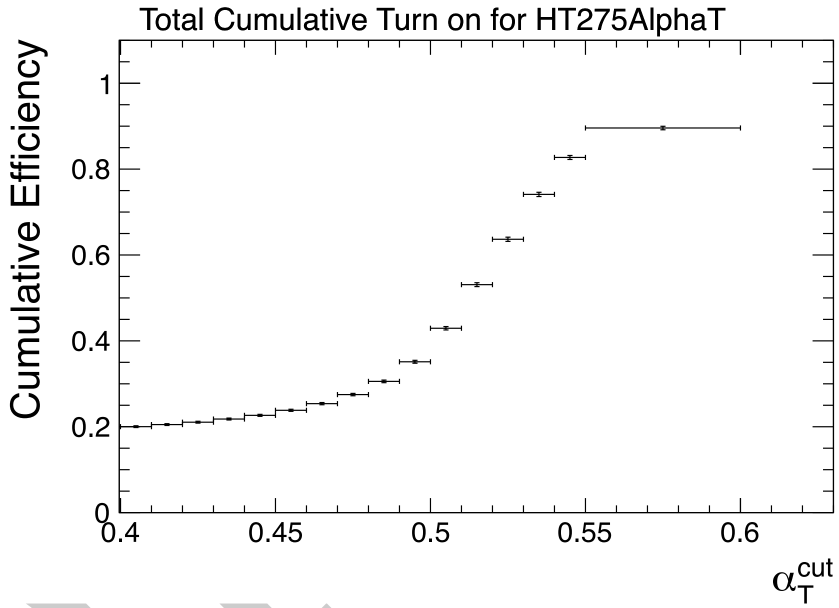

Figure 6.10: Combined cumulative efficiency for the triggers seeding the 275 GeV $< H_\mathrm{T} <$ 325 GeV offline bin for 11.7 fb^{-1} of 8 TeV LHC data.

6.6 Electro-Weak background prediction

The requirement of an α_T cut on the signal sample removes multi-jet QCD events where a balanced event is counted as signal due to miss-measurements, the remaining background events in the signal region are due to electro-weak processes which produce real missing energy. Primarily these events are produced from $\mathrm{Z} \rightarrow \nu\overline{\nu}$ + Jets, $\mathrm{W} \rightarrow \ell\overline{\nu}$ + Jets and $\mathrm{t\bar{t}}$ decay, with smaller contributions from Drell-Yan + Jets, single top production in the s,t and tW channels and from di-boson + Jet events. To predict the number of these events contribution to the number of signal events three control samples are defined and though the use of a montecarlo derived transfer factor the control samples are used to predict the number of S.M events expected in the signal region.

Figure 6.11[2] shows the expectation from simulation in all bins of the hadronic signal region, for the different background samples and an example CMSSM reference model RM1.

Expalin what RM1 is

The expected composition of the the backgrounds in the hadronic signal region, as a percentage of the total S.M background, are summarised in Table 6.6. $\mathrm{Z} \rightarrow \nu\nu$ contributes ≈43% of the S.M background in the 275 GeV–325 GeV H_T bin, raising to ≈53% in the $H_\mathrm{T} > 875$ GeV bin. Events entering the signal region due to Z or W decays where the lepton is missed by the lepton vetoes account for ≈25% at low H_T and ≈13% at high H_T. Events from hadronicly decays τ (τ_h) have a low H_T dependance, contributing ≈22% of the background at low H_T and ≈27% of the background at high H_T. Those events arising from τ particles which decay leptonically (τ_l) and are missed by the lepton vetoes account for ≈10% of the S.M background.

To calculate the bin by bin translation factors the signal selection and the individual control selections are applied to the montecarlo simulated background samples. The ratio of the number of accepted events is then taken, the signal yield prediction is computed from applying the the control selections to real data and multiplying the event yield by the translation factor. The measurements form all control samples are considered simultaneously in a fit defined in Section 6.10. This method can be extended to high dimensions of analysis bins, for example in [3] a secondary dimension involving the number of B quarks in the event is studied. However the B extension is not detailed in this thesis.

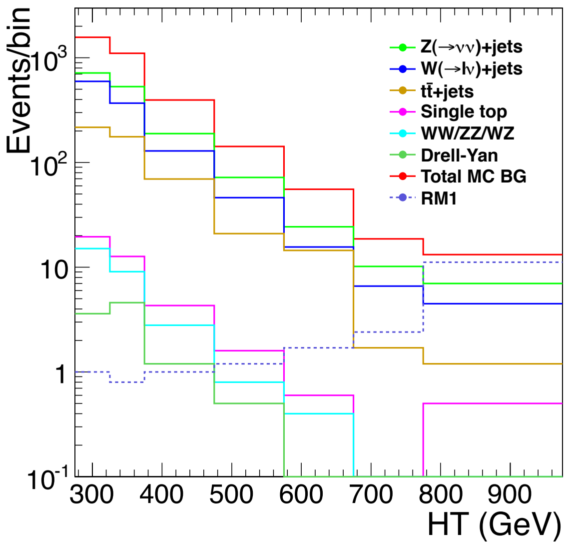

Figure 6.11: Expectation from MC in all bins of the hadronic signal region for the following different background processes: $Z \to \nu\nu$ + jets, W + jets, $t\bar{t}$, single top + jets, di-boson production (WW/WZ/ZZ), and Drell-Yan. The total SM expectation is also shown, along with that for the CMSSM benchmark model RM1.

Table 6.6: Relative background composition as given by MC simulation in all bins of the hadronic signal region (expressed as a percentage of the total SM background).

H_{T} GeV	$\mathrm{N}_{\mathrm{events}}$	$Z \to \nu\nu$ + jets (%)	W + jets, $t\bar{t}$, single top, DY and di-boson			
			missed e, μ from W/Z (%)	τ_h (%)	τ_l (%)	τ_h matched to jet (%)
275–325	3938.0	43	24	22	11	7
325–375	1569.9	46	25	22	9	7
375–475	1104.2	48	20	23	10	7
475–575	396.0	48	17	24	11	10
575–675	142.4	51	17	23	10	11
675–775	55.5	44	19	31	7	17
775–875	18.7	55	17	22	4	9
875–∞	13.2	53	13	27	7	19

$$N^{sig}_{prediction}\left(H_{\mathrm{T}}\right) = N^{control}_{obs}\left(H_{\mathrm{T}}\right) \times \frac{N^{sig}_{MC}\left(H_{\mathrm{T}}\right)}{N^{control}_{MC}\left(H_{\mathrm{T}}\right)} \tag{6.9}$$

The three control samples used are a W $\rightarrow \mu\overline{\nu}$ + Jets sample, a Z $\rightarrow \mu\mu$ + Jets sample and a γ + Jets sample.

The selection criteria for each of these control samples is kept as similar to the signal selection as possible, so as to not introduce systematic errors from incorrect modelling in the simulation. The use of the ratio of the number of observed events in the montecarlo cancels the systematic effects. A systematic is still assigned to each translation factor to account for theoretical uncertainties and acceptance and instrumental effects.

Additional kinematic cuts are applied in the two muon control samples to enrich the W + Jets $t\bar{t}$ and Z + Jets components in the control samples. The samples are defined to maximised efficiency rather than purity, any impurities are accounted for in the transfer factors as the yields from all montecarlo samples are used. This is valid under the assumption that the S.M electro-weak and Drell-Yan processes are well modelled by the simulation. The possibility of SUSY like signal contamination in the control samples is accounted for in the final likelihood, after measuring the signal acceptance for the control samples on simulated SUSY events.

The magnitude of the systematic uncertainties on the transfer factors is motivated by a set of closure tests between the control samples. A transfer factor is produced to predict each control sample from each of the other control samples. No assumed systematic is applied in these closure tests, instead the level of agreement with in statistical uncertainty is used to set the scale of the systematic error for each H_{T} bin.

The μ + Jets control sample The μ + Jets control sample is designed to mimic the events appearing in the signal region due to W + Jets and $t\bar{t}$ decays where the leptons are missed offline, either due to falling out of acceptance or being missed by the reconstruction algorithms. Hadronic tau decays from high p_{T} W bosons are also predicted from this sample. The additional selection criteria for this sample are designed to select events containing the decay W $\rightarrow \mu\nu$ + Jets in the same kinematic conditions as those events entering the signal selection. Offline the event level discriminators, H_{T} and α_T, are calculated using only the hadronic components of the event. In order to select the W exactly one tightly identified, isolated muon with in $|\eta| < 2.5$ with $p_{\mathrm{T}} >$ 10 GeV is required. The transverse mass of the muon combined with the missing energy of the event $M_T(\mu, \not{E}_{\mathrm{T}})$ is required to be larger than 30 GeV, as shown in Figure 6.12 the transverse mass cut removes a large amount of QCD whilst preserving a high efficiency W selection. Events are vetoed if for any jet $\Delta R(\mu, Jet) < 0.5$, or if a second muon candidate exists that is either loose, non-isolated or outside of acceptance if the two muons have an invariant mass with in ±25 GeV of the Z mass, to suppress $Z \rightarrow \mu\mu$ events.

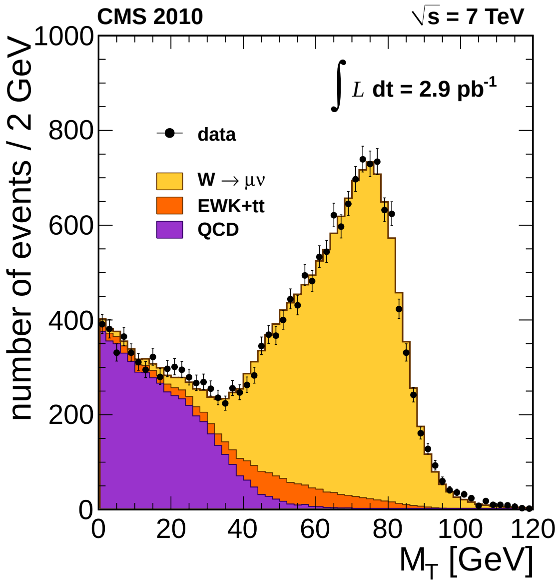

Figure 6.12: Transverse mass between the selected muon and $\not{E}_T$ in $W \rightarrow \mu\nu$ events.[1].

The $\mu\mu$ + Jets control sample The $\mu\mu$ + Jets control sample is used to measure the $Z \rightarrow \nu\nu$ + Jets irreducible background in the signal region. The process $Z \rightarrow \mu\mu$ + Jets is identical kinematically, however the acceptance and the branching ratio are both smaller the branching ratio due to the possible decay in to one of three neutrino flavour states verses the requirement of a particular lepton flavour, the acceptance difference is due to the p_T and identification quality requirements on the muons alter the acceptance between the two processes. The following selection criteria are applied on top of the common selection: Exactly two tightly identified, isolated muons, with in $|\eta| < 2.5$ with $p_T > 10$ GeV are required; The invariant mass of the di-muon pair is required to be with in ±25 GeV of the Z mass; Events are vetoed if for any muon and jet combination $\Delta R(\mu, Jet) < 0.5$. As in the single muon control sample all event level quantities are calculated from the hadronic objects alone. This control sample can be used in all of the offline H_T bins.

The γ + Jets control sample The γ + Jets control sample can also be used to measure the $Z \rightarrow \nu\nu$ + Jets background as the γ + Jets process is kinematically similar when the γ $E_{\mathrm{T}} > \approx 100$ GeV[12, 7], again when calculating the event level quantities only hadronic objects are considered. The photon sample requires the following criteria on top of the common selection requirements: Exactly one photon with $E_{\mathrm{T}} > 150$ GeV to ensure trigger efficiency, $|\eta| < 1.45$. Events are vetoed if for any jet $\Delta R(\gamma, jet) < 1.0$. Given that due to the trigger requirements the photon E_{T} is required to be greater than 150 GeV and the photon is treated as missing energy, the $\alpha_T > 0.55$ requirement implies a minimum H_{T} threshold of ≈ 350 GeV, hence the γ + Jets control sample can only be used in the offline region where $H_{\mathrm{T}} > 375$ GeV.

Table 6.7 gives the hadronic signal yields in each of the offline H_{T} bins along with the simple background estimate from the single muon plus jets control sample. The full background prediction is given from the results of the simultaneous fit to the separate background estimates.

Table 6.7: Total SM prediction using the μ + Jets sample only. These are illustrative only, as the final prediction is provided by the final simultaneous fit.

α_T bin	0.55–∞	0.55–∞	0.55–∞	0.55–∞
H_{T} bin (GeV)	275–325	325–375	375–475	475–575
Hadronic selection MC	2872.32 $\pm$ 64.44	1384.22 $\pm$ 51.46	1041.38 $\pm$ 12.53	396.13 $\pm$ 19.85
μ+ jets selection MC	1228.90 $\pm$ 46.18	670.50 $\pm$ 38.74	495.14 $\pm$ 7.86	181.65 $\pm$ 9.65
Translation factor	2.34 $\pm$ 0.10	2.06 $\pm$ 0.14	2.10 $\pm$ 0.04	2.18 $\pm$ 0.16
μ+ jets selection yield data	1421	645	517	169
Total SM prediction	3321.30 $\pm$ 169.97	1331.57 $\pm$ 105.45	1087.36 $\pm$ 52.50	368.56 $\pm$ 39.09
Hadronic yield data	3703	1533	1043	346

α_T bin	0.55–∞	0.55–∞	0.55–∞	0.55–∞
H_{T} bin (GeV)	575–675	675–775	775–875	875–∞
Hadronic selection MC	142.37 $\pm$ 7.61	55.47 $\pm$ 3.51	18.68 $\pm$ 1.45	13.18 $\pm$ 1.15
μ+ jets selection MC	70.84 $\pm$ 4.36	22.64 $\pm$ 1.82	7.54 $\pm$ 0.80	5.19 $\pm$ 0.67
Translation factor	2.01 $\pm$ 0.16	2.45 $\pm$ 0.25	2.4 $\pm$ 0.33	2.54 $\pm$ 0.40
μ+ jets selection yield data	52	18	8	1
Total SM prediction	104.50 $\pm$ 16.81	44.09 $\pm$ 11.33	19.83 $\pm$ 7.41	2.54 $\pm$ 3.47
Hadronic yield data	122	44	14	6

Muon control samples with out an α_T cut. The requirement of an α_T value above 0.55 in the previous control samples limits the even yield of each of the montecarlo samples, increasing the statistical error of the prediction. This is especially evident when splitting the analysis in to more dimensions than the H_{T} binning. The requirement of an

α_T cut on the control samples means that as the muon is not seen by the calorimeter systems the signal trigger can also be used to collect the both the single and di muon background samples. The translation factor method can be used to create a prediction from any sample to any other sample if and only if the modelling of the even kinematics and acceptances of any cuts introduces no large systematic errors. We now show that the montecarlo simulation accurately reproduces the kinematics and acceptance of the α_T cut when applied to electro-weak background samples, enabling the removal of the α_T requirement for the muon control samples.

The preselection of events in the two muon control samples ensures samples with negligible QCD contamination, which are enriched with $t\bar{t}$, W + Jets and Z + Jet events. This is shown for the μ^- + Jets sample in Figure 6.13 and for the $\mu^-\mu^+$ + Jets sample in Figure 6.14, in both sets of plots the expected number of QCD events from montecarlo simulation is less than one even at any α_T value for 5 fb^{-1} of integrated luminosity. The requirement of tight isolation on each of the muons is largely responsible for the purity of the sample, the transverse mass and di-muon mass window cuts ensure the sample is rich in electro-weak events with visible muons.

Moving to a selection where there is no required α_T cut means that the α_T trigger suite can not be used to collect the high event yield control samples. Instead a trigger requiring H_T and a muon in the final state (`Mu_HT`) is used, due to the muon trigger threshold the p_T acceptance cut is raised to 45 GeV in these control samples. The H_T requirement on these triggers raises to 300 GeV so only the offline bins with $H_\mathrm{T} >$ 375 GeV are able to benefit from the increased background estimation precision, due to the larger size of the predicting sample. The efficiency for triggering on a single muon at 45 GeV is measured to be 91.3±0.1% though out the data taking period, measured for the H_T + single muon triggers, the H_T component of the trigger is measured to be 100% efficient though out. In the case of the di-muon sample, as both muons have to be above 45 GeV and either of them could have triggered the event, the efficiency is found to be H_T-dependant in the range of 95-97%.

The muon control samples in the H_T bins where $H_\mathrm{T} <$ 375 GeV are collected with the α_T trigger suite and the measured efficiencies are the same as those measured for the hadronic sample. The details of the triggers used for each of the muon + Jets control samples are listed in Table 6.8.

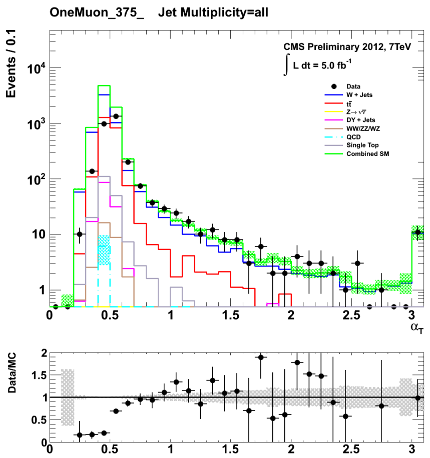

(a) α_T distribution (see main caption).

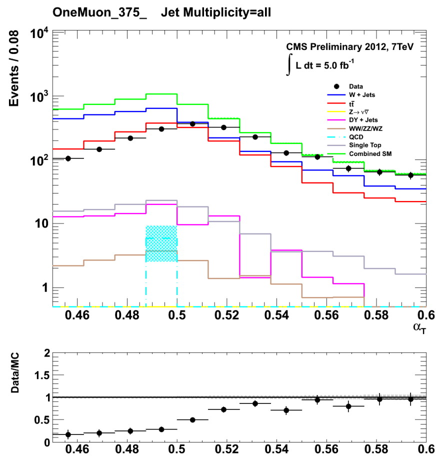

(b) Zoomed α_T distribution (see main caption).

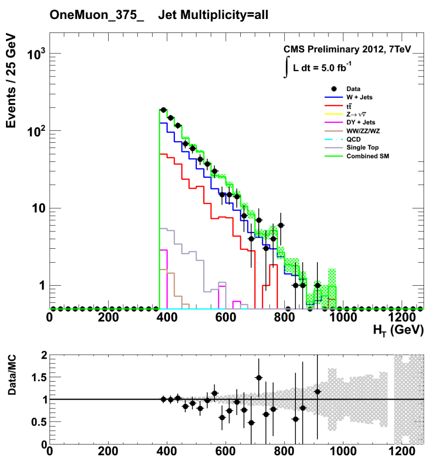

(c) H_{T} distribution.

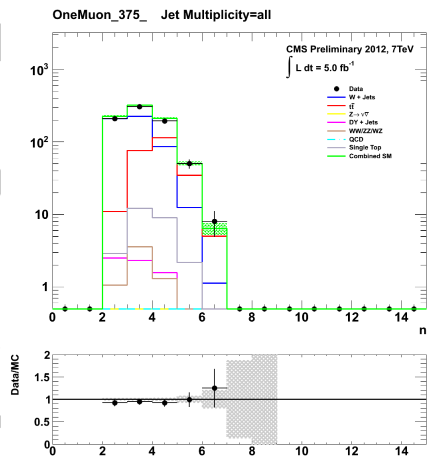

(d) N_{jet} distribution.

Figure 6.13: Data–MC comparisons of key variables for the muon control sample, for the region $H_{\mathrm{T}} > 375$GeV and $\alpha_T > 0.55$. Bands represent the uncertainties due to the limited size of MC samples. No requirement is made on the number of b-tagged jets in an event. *The discrepancy in the α_T distributions for values $\alpha_T > 0.55$ is due to the trigger not being simulated in the MC simulation.*

6.7 Estimating the residual QCD background component.[2]

The expected QCD contamination in the signal region where $H_{\mathrm{T}} > 275$ GeV and $\alpha_T >$ 0.55 from simulated background samples is negligible, residual events are removed via the application of the detector failure and $R_{miss} < 1.25$ filters. However due to the difficulty

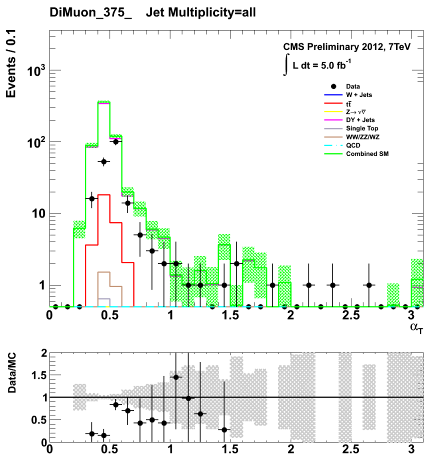

(a) α_T distribution (see main caption).

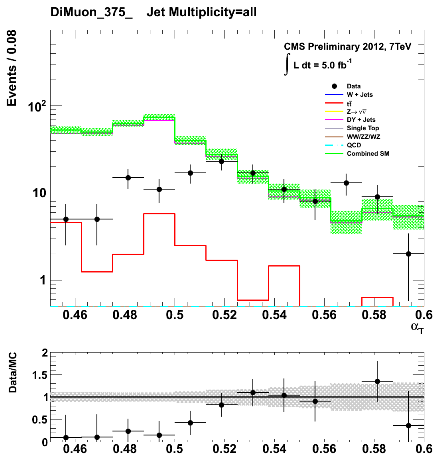

(b) Zoomed α_T distribution (see main caption).

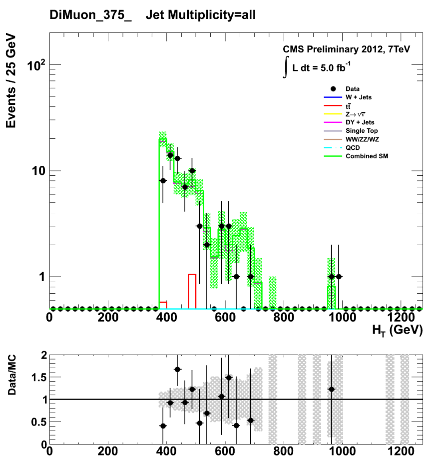

(c) H_{T} distribution.

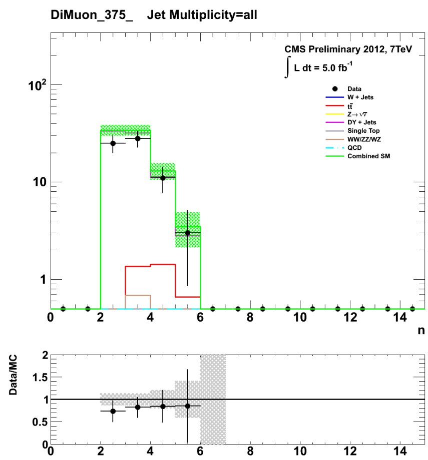

(d) N_{jet} distribution.

Figure 6.14: Data–MC comparisons of key variables for the di-muon control sample, for the region $H_{\mathrm{T}} > 375$GeV and $\alpha_T > 0.55$. Bands represent the uncertainties due to the limited size of MC samples. No requirement is made on the number of b-tagged jets in an event. *The discrepancy in the α_T distributions for values $\alpha_T > 0.55$ is due to the trigger not being simulated in the MC simulation.*

in simulating QCD multi jet events accurately a conservative approach is taken where a term is inserted in the likelihood to model any residual QCD contamination.

The term is based on the ratio of the number of events above and below the α_T threshold of 0.55 in the individual H_{T} bins. The dependance of this ratio is modelled as an exponentially falling quantity:

$$R_{\alpha_T}(H_{\mathrm{T}}) = \mathcal{A}_{n_b} e^{-k_{QCD} H_{\mathrm{T}}} \tag{6.10}$$

Table 6.8: List of triggers used for the larger μ + jets and $\mu\mu$ + jets samples.

H_{T} bin (GeV)	275–325	325–375	375–475	475–575	575–675	675–775	775–875	>875
α_T cut	0.55	0.55	None	None	None	None	None	None
Muon p_{T} cut	10	10	45	45	45	45	45	45
Trigger	α_T	α_T	`Mu_HT`	`Mu_HT`	`Mu_HT`	`Mu_HT`	`Mu_HT`	`Mu_HT`
Dataset	`HT`	`HT`	`MuHad`	`MuHad`	`MuHad`	`MuHad`	`MuHad`	`MuHad`
Thresholds	Table 2	Table 2	Table 3	Table 3	Table 3	Table 3	Table 3	Table 3

Where $\mathcal{A}_{n_b}$ is the b-tag bin dependant normalisation factor and k_{QCD} is the b-tag dependant decay constant.

The exponential behaviour is due to several features, the first of which is the improvement of the jet energy resolution with H_{T} due to the larger energies deposited in the calorimeter systems.

find CMS JET ENERGY RESOLUTION PLOT JETMET PAS???

Secondly for the region $H_{\mathrm{T}} > 375$ GeV the jet multiplicity rises slowly with H_{T}, which due to the combinatorics used in the α_T calculation, results in a narrower α_T distribution peaked at 0.5. Due to the signal region definition and the exponentially falling nature of the QCD background component is reduced to zero above ≈ 500 GeV, thus the validity of the QCD background model above 575 GeV is not of consequence to the final analysis, however the model chosen is shown to be valid over the whole H_{T} region of the analysis as shown below.

Maximum likelihood (M.L) values for k_{QCD} and $\mathcal{A}_{n_b}$ are found by the final likelihood fit, however k_{QCD} is first constrained by a measurement in a background enriched side band regions where either the α_T cut is relaxed or the R_{miss} cut is inverted. Figure 6.15 depicts the regions where k_{QCD} is measured, the signal region is as described before where $\alpha_T > 0.55$ and $R_{miss} < 1.25$ are required. Region B is defined by the inversion of the α_T cut. Region C is defined by inverting both the α_T requirement and the R_{miss} requirement, this region is further divided in to three slices in α_T of $0.52 < \alpha_T < 0.53$, $0.53 < \alpha_T < 0.54$ and $0.54 < \alpha_T < 0.55$, as the index of C_i rises the expected amount of QCD in that control region increases. Finally region D has only the R_{miss} requirement inverted, region D is not used to constrain k_{QCD}, but instead to check the validity of the exponential model. The fits to the individual side bands are shown in Appendix 2. The best fit value for k_{QCD} of $2.96 \pm 0.64 \times 10^{-2}$ GeV^{-1} obtained from region B is used as the central value of the constraint. The assumption that this method gives an unbiased

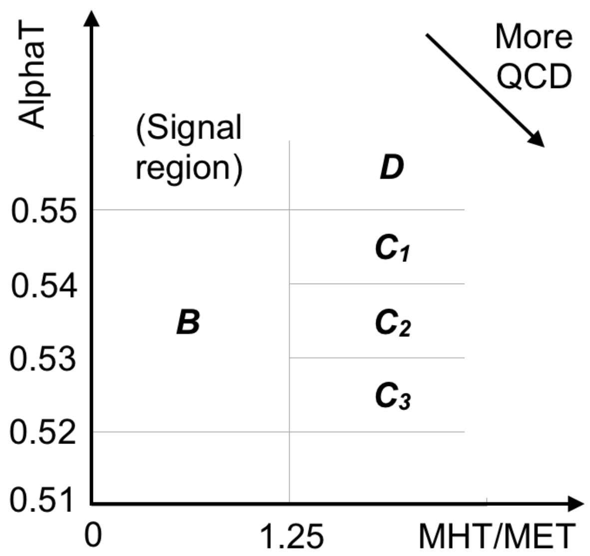

Figure 6.15: QCD side-band regions, used for determination of k_{QCD}.

estimate of k_{QCD} stems from the similarity in event kinematics in the two α_T regions. The best fit values for the three C_i regions are used to estimate the systematic uncertainty on the central value obtained from region B. The fit results show now dependance on the α_T region used to measure the number of events, supporting the assumption that region B provides an unbiased estimate of k_{QCD}. The variation of the measured values for each C_i slice are used to calculate the error on the central value, the weighted mean and standard deviation of the three slices in α_T are calculated to be $1.13 \pm 0.26 \times 10^{-2}$ GeV^{-1}, the relative error on this value is 20% which is then applied to the central value to give an estimate of the systematic uncertainty.

The data side bands are used to provide a constrained value of k_{QCD} as an input to the final likelihood model which describes the expected number of background events in bins of H_{T} and the number of observed jets containing a b quark. The value measured for k_{QCD} is $2.96 \pm 0.61(\text{stat}) \pm 0.46(\text{sys}) \times 10^{-2}$ GeV^{-1}. The uncertainty values are used as penalty timers in the likelihood model which is described in Section 6.10

A final check is performed using region D, which requires $\alpha_T > 0.55$ but has no R_{miss} cut, this introduces QCD background in to the signal region. The likelihood fit is performed on this background enriched region and no constraint is applied on k_{QCD} which is then determined by the fit only. The fit is performed over the full H_{T} range used in the final analysis. Figure 6.16 shows the resulting fit, the M.L value obtained for k_{QCD} is $(1.31 \pm 0.09)\times 10^{-2}$ GeV^{-1}, this value is in excellent agreement with the value

Table 6.9: Best fit values for the parameters k as obtained from the regions B, C_1, C_2, and C_3. The latter three measurements are used to calculate a weighted mean (identified as region C). Also quoted is the maximum likelihood value of the parameter k given by the simultaneous fit using the sample defined by region D. Quoted errors are statistical only. From [2].

Side-band region	k_{QCD} ($\times 10^{-2}$ GeV^{-1})	p-value
B	2.96 ± 0.64	0.24
C_1	1.19 ± 0.45	0.93
C_2	1.47 ± 0.37	0.42
C_3	1.17 ± 0.55	0.98
C (weighted mean)	1.31 ± 0.26	-
D (likelihood fit)	1.31 ± 0.09	0.57

found from the weighed mean of the regions C_i, secondly the fit shows that the choice of exponential function used in the likelihood model is valid over the entire H_{T} range. This supports the assumption that region B provides an unbiased estimate of k_{QCD} in the signal region $\alpha_T > 0.55$ and $R_{miss} < 1.25$.

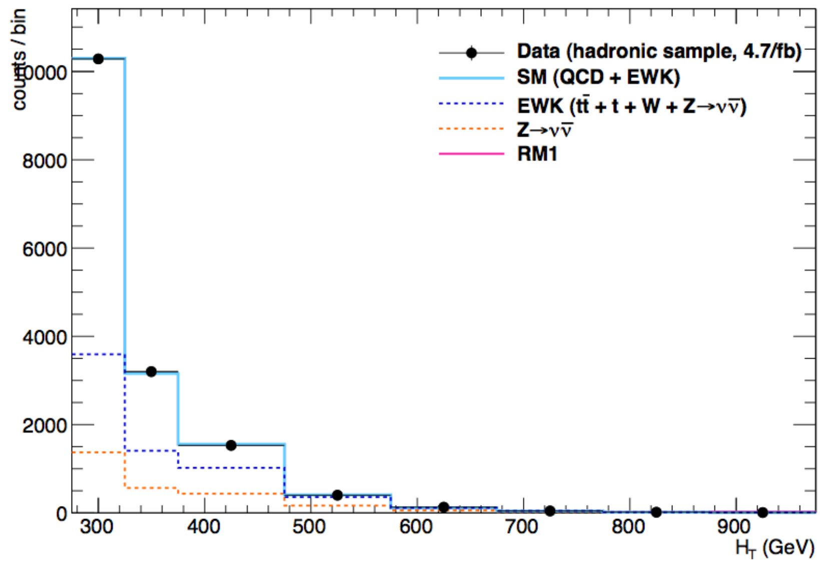

Figure 6.16: Comparison of the observed yields and SM expectations given by the simultaneous fit in bins of H_{T} for the side-band region D. No requirement on the number of b jets is made. Shown are the observed event yields in data (black dots with error bars representing the statistical uncertainties) and the expectations given by the simultaneous fit for the Z $\rightarrow \nu\nu$+jets process (orange dotted-dashed line); the sum of all processes with genuine $\not{E}_{\mathrm{T}}$, which are primarily $\mathrm{t\bar{t}}$, W+jets, and Z $\rightarrow \nu\nu$+jets (dark blue long-dashed line); and the sum of QCD and all aforementioned SM processes (light blue solid line).[2]

6.8 Systematic uncertainties on the electro-weak background model.

As previously discussed in Section 6.6 the final background prediction is given by the simultaneous fit to the yields in the signal and control samples and the translation factors obtained from MC. The fit has some freedom via the statistical and systematic uncertainties measured for each translation factor. This implies that the measurement of the systematic uncertainties on the translation factors are vital for the fitting procedure.

A set of closure tests were performed on data to identify any sources of systematic biased introduced by the background prediction method. To do this the individual background samples are used to predict one another using the same translation factor method as for the prediction of S.M missing energy sources in the hadronic signal regions. The level of agreement is quantified in terms of the ratio $(N_{obs} - N_{pred})/N_pred$, the statistical error from the translation factor, based on the available Montecarlo statists is combined with the statistical error on the number of events in the predicting sample to give the error on the closure, hence the deviation of the ratio from zero gives the level of closure per analysis bin. This gives a measure of any biases introduced by the background estimation method.

The closure tests between the background samples are designed to test the Montecarlo's ability to model kinematic effects; such as the α_T acceptance; μ^- acceptance and γ acceptance, instrumental effects such as; reconstruction efficiencies and the effects of pile up on isolation and finally the theoretical precision of the production and decay cross sections and their relative contributions to the S.M background. These individual components are not separable by the closure tests, which instead gives a total systematic error estimation.

As described in Section 6.6 the control samples which do not require an α_T cut use a `Mu_HT` cross object trigger to collect the data events. As shown in Table 3 there was a period of data taking where due to the increased trigger thresholds the `Mu_HT` triggers are unsuitable for use in the region $H_\mathrm{T} < 375$ GeV. Thusly in the closure tests between the control samples which use an α_T cut and those that do not the integrated luminosity is limited to 3.9 fb^{-1}. This causes a loss of some statistical power in these cases.

The individual closure tests and fits to the H_T dependance of the ratio $(N_{obs} - N_{pred})/N_pred$ are shown in Appendix 3. The Figures 6 show the closure of the prediction between $\mu +$

jets (no α_T) $\rightarrow$ μ + jets ($\alpha_T > 0.55$) and $\mu\mu$ + jets (no α_T) $\rightarrow$ $\mu\mu$ + jets ($\alpha_T > 0.55$) for two samples, one with no requirement on the number of b tagged jets (n_b), which increases the precision of the measurement, and one requiring $n_b = 1$, the read line is the result of a one parameter fit. The level of closure shows that the Montecarlo accurately models the α_T acceptance, with no significant bias.

Figure 7 shows the closure between μ + jets $\rightarrow$ $\mu\mu$ + jets and between γ +jets $\rightarrow$ $\mu\mu$ + jets over both the full H_{T} range using only 3.9 fb^{-1} of integrated luminosity and for $H_{\mathrm{T}} > 375$ GeV using the full data set. Again the red lines are the result of fitting with a one parameter fit.

Figure 8 tests the closure between samples with differing n_b the three tests are μ + jets ($n_b = 0$)$\rightarrow$$\mu$ + jets ($n_b = 1$,no α_T), μ + jets ($n_b = 1$)$\rightarrow$$\mu$ + jets ($n_b > 1$,no α_T) and μ + jets ($n_b = 0$)$\rightarrow$$\mu$ + jets ($n_b > 1$,no α_T). Figure 9 also tests the closure between samples with differing n_b, here the test is between μ + jets ($n_b = 0$)$\rightarrow$$\mu\mu$ + jets ($n_b = 0$) and μ + jets ($n_b = 1$)$\rightarrow$$\mu\mu$ + jets ($n_b = 1$).

Finally any dependance on pile up is measured by comparing a subset of the individual closure tests between samples which have pile up subtracted jets and those that do not. The example closures are μ + jets (no α_T)$\rightarrow$$\mu$ + jets ($\alpha_T > 0.55$), μ + jets (no α_T)$\rightarrow$$\mu\mu$ + jets (no α_T), and μ + jets ($n_b = 0$)$\rightarrow$$\mu$ + jets ($n_b = 1$,no α_T).

6.8.1 Motivating the combined systematic on the translation factors

The closure tests described in the previous section are combined to give a total systematic uncertainty. This uncertainty is binned in to three H_{T} regions 275 GeV$\rightarrow$575 GeV, 575 GeV$\rightarrow$775 GeV and 775 GeV+. In each of these regions all of the individual closure tests are used to calculate a weighted mean and variance. The systematic is defined as 3σ of this variance, which is conservative but necessary to cover any biases. The systematics are treated as fully uncorrelated between the three regions, again this is the conservative approach. Figure 6.17 shows the key example closures, the grey shaded region shows the systematic error. The values obtained for the error are 6%, 20% and 39%, these are rounded to 10%, 20% and 40% and then used in the final background simultaneous fit.

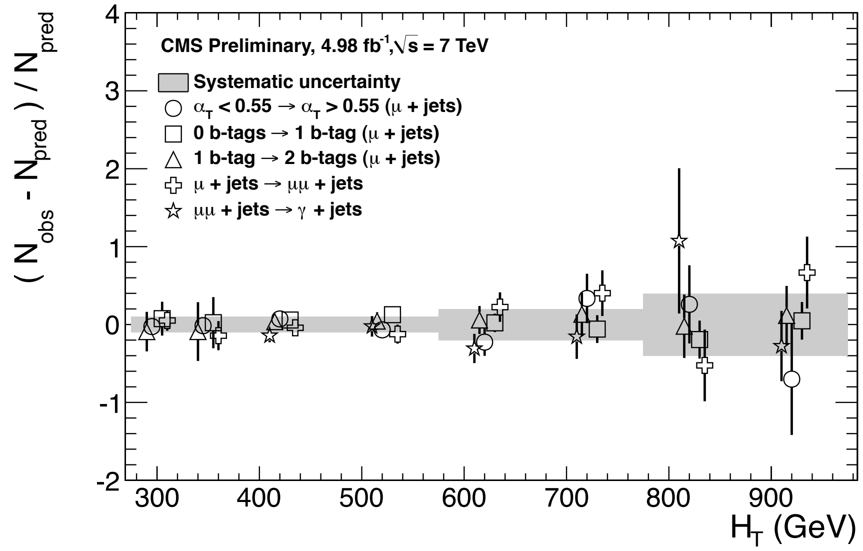

Figure 6.17: A set of closure tests (open symbols) overlaid on top of grey bands that represent the systematic uncertainties used for three H_{T} regions in the final simultaneous fit. The solid circles and their errors represent the weighted mean and standard deviation for the five closure tests of each individual H_{T} bin.

6.9 Signal Models

The level of agreement of the analysis with the S.M give a handle on the production cross sections and masses of particles predicted by new physics models. The final results are presented in terms of a specific SuperSymmetry (SUSY) model and a selection of generic final state topologies, known as Simplified Model Spectra (S.M.S).

The SUSY model considered is the Constrained Minimal SuperSymmetric Model (CMSSM)[] which is described in Section 2.1, the parameters chosen are $\tan\beta = 3, \mathcal{A}_0 =$ $, \mu =$ with the exclusion curve presented in the m_0, $m_{1/2}$ plane. This model combines many production and decay topologies and is common to results shown by previous and contemporary experiments []

Reference ATLAS and Tevatron susy results

. The results are also presented in terms of S.M.S[] models, these are models with single production methods and a specified decay topology. The C.M.S terminology for the production methods are as follows: T1 models are gluino-gluino production, which then decay to four S.M hadronic jets and two neutrilinos. T2 models are squark-squark production with decays to two S.M hadronic jets and two neutrilinos. These topologies can be further specialised by enforcing the squarks or gluinos to decay to heavy flavour S.M quarks, such as t, which promptly decay to jets containing b quarks or direct decays to b quarks. The limits on the S.M.S space are defined in terms of the mass splitting between the neutrilino and the pair produced SUSY particle defining the model.

6.9.1 Signal Efficiency

CMSSM The CMSSM signal scan is composed of eight sub-processes which define the production and decay topologies. The dominant process varies with $m_0, m_{1/2}$ and at next to leading order the cross section for each of theses processes varies per point. The analysis is run over each sub process in turn with the final efficiency given by the weighted sum of the subprocess efficiencies. The yield per point is then given by $\epsilon \times \mathcal{L}$ for 5 fb^{-1} the total yields are show in the appendix in Figure 11 these yields are for the sum of the H_{T} analysis bins.

Simplified Models The S.M.S models contain only one production process and a set decay topology, making the interpretation in these models simpler, however the individual models are not representative of some complete SUSY model. Instead these models allow the testing of specific facets of new physics models, with out the ambiguity of the relative contributions of each sub process at a point which is seen when testing full models. The efficiency is measured for each of the models, with the yield per point given by $\epsilon \times \sigma \times \mathcal{L}$ where σ is given as a reference cross section only. The efficiencies for which are shown in the appendix, Table 6.10 lists which figure corresponds to which model, it is to be noted that the total efficiency summed over H_{T} bins is shown.

Table 6.10: Production and decay modes for various simplified models.

Model	Production and decay modes	Figure showing efficiency
`T1`	$\tilde{\mathrm{g}}\tilde{\mathrm{g}} \rightarrow q\bar{q}\tilde{\chi}^0 q\bar{q}\tilde{\chi}^0$	12
`T2`	$\tilde{q}\tilde{q} \rightarrow q\tilde{\chi}^0\bar{q}\tilde{\chi}^0$	13
`T2tt`	$\tilde{\mathrm{t}}\tilde{\mathrm{t}} \rightarrow \mathrm{t}\tilde{\chi}^0\bar{\mathrm{t}}\tilde{\chi}^0$	14
`T2bb`	$\tilde{\mathrm{b}}\tilde{\mathrm{b}} \rightarrow \mathrm{b}\tilde{\chi}^0\bar{\mathrm{b}}\tilde{\chi}^0$	15
`T1tttt`	$\tilde{\mathrm{g}}\tilde{\mathrm{g}} \rightarrow \mathrm{t}\bar{\mathrm{t}}\tilde{\chi}^0\mathrm{t}\bar{\mathrm{t}}\tilde{\chi}^0$	16
`T1bbbb`	$\tilde{\mathrm{g}}\tilde{\mathrm{g}} \rightarrow \mathrm{b}\bar{\mathrm{b}}\tilde{\chi}^0\mathrm{b}\bar{\mathrm{b}}\tilde{\chi}^0$	17

Signal Efficiency for the Background Selection If the couplings of the SUSY particles are analogous to the S.M particles then the final states may involve muons which in the presence of signal would infer an over estimation of the background from the control samples. To measure this the background selection is applied to the signal models and the yields are taken into account in the final limit setting procedure. On average the background selection's efficiency on signal is 10× lower than the efficiency in the hadronic signal region. This is shown for the model `T1tttt` in Figure 18 where the most muons of all the signal models are expected in the final state, the contamination in the n_b bins that drive the limit is on the order of $10 - 20\%$.

6.9.2 Uncertainty on Signal Efficiency

The systematic uncertainty on the signal models is due to: Choice of Parton Density Function (PDF) at generator level, the PDF set used to generate the sample has effects on both the acceptance and the cross section; The measurement of the integrated luminosity is accounted for in the signal yield; Due to the signal models being created with C.M.S FastSim[] rather than C.M.S FullSim[] the acceptance differs between the signal and the background samples; The error on the jet energy scale is accounted for on the signal yield; Systematic errors from the cleanings cuts (R_{miss} and ECAL dead regions) and lepton/photon vetoes are also taken in to account; Finally corrections to the b-tagging efficiency between the FullSim and the FastSim are applied as well as their errors.

Each of these uncertainties is expressed as a percentage change in the efficiency from the central value given by applying the full analysis to each signal model, the total systematic is given by summing the components in quadrature. In the following section the measurements of the error from each of these sources is detailed and summarised per considered signal model at the end of the section.

The uncertainties for the CMSSM are considered in a band of ±60 GeV in $m_{1/2}$ around the expected limit to confine the errors to the relevant part of the plane, in the very high $m_0, m_{1/2}$ area the jet energy scale causes large fluctuations due to the small mass splitting between the SUSY particles. For the S.M.S models two regions are defined, one "close" to the diagonal, which has small mass splitting and thus the effects of jet energy scale and PDF acceptance have a large impact on the analysis efficiency. A second "far" region is defined with large mass splitting and thus a small change on the analysis efficiency due to jet energy scale and PDF variations. The near and far regions are defined by:

$$m_{sq}(m_{gl}) - m_{lsp} > 350 \text{ GeV}\&\& m_{sq}(m_{gl}) > 475 \text{ GeV} \tag{6.11}$$

events passing these conditions are classified as being in the "far" region, those failing in the "close" region.

Choice of PDF set at generator level.

The PDF set contains information on the interaction probabilities of the quark and gluons in the proton at different energies, the model used in the production of the Montecarlo simulation has direct impact on the kinematics of the final states, since the PDFs have been measured at lower energies than those found at the Large Hadron Collider (L.H.C) the quark and gluon distributions have been extrapolated from the low energy regime, the uncertainty at high energy is thus significant. The uncertainties on acceptance due to the choice of PDF set used to generate the signal Montecarlo are calculated in line with the `PDF4LHC`[8] working group recommendations. On the event level the individual weights are re-calculated by moving between PDF set, the weight is based on the energy at which the quarks or gluons interaction and the form given by the PDF. This is done for the central value of the three considered PDF sets (CTEQ6.1[22], MSTW2008nlo68cl[23] and NNPDF2.0[24]) and for the variations of each of their errors. The change in analysis efficiency is measured per H_{T} bin, Figure 6.18 shows

the deviation in efficiency per bin for three examples points in the CMSSM plane, the error bars represent the RMS of the spread of the efficiency inside each PDF set. It is to be noted that some bins show a large change in efficiency due to the choice of PDF set, however these are low efficiency bins where changes in yield of a few events has a large effect, the final result however is driven by the high efficiency bins, hence these large fluctuations can be ignored. The effects on the cross section are studied by re-calculating the Next to Leading Order (N.L.O) cross sections of each of the sub processes for each choice of PDF set, this is done centrally by C.M.S, these changes in cross section are accounted for in the error band on the expected limit.

6.10 Likelihood model

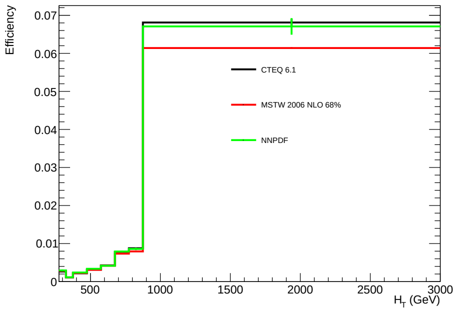

(a) $m_0 = 200\ GeV, m_{1/2} = 500\ GeV$

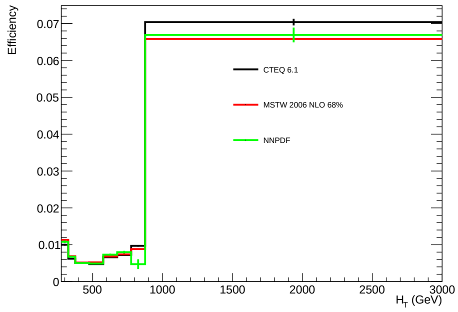

(b) $m_0 = 500\ GeV, m_{1/2} = 500\ GeV$

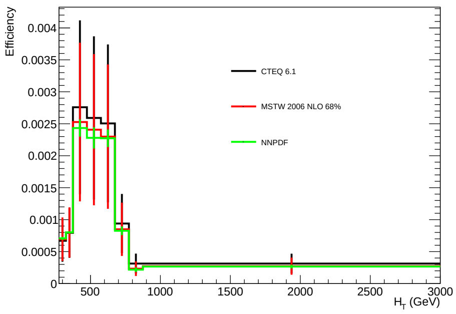

(c) $m_0 = 200\ GeV, m_{1/2} = 1800\ GeV$

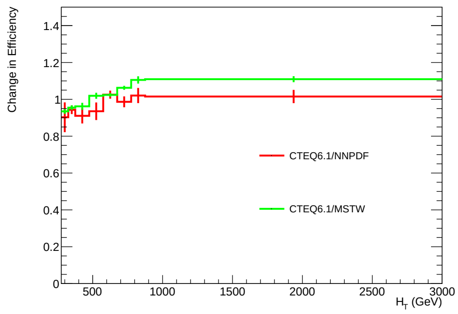

(d) $m_0 = 200\ GeV, m_{1/2} = 1800\ GeV$

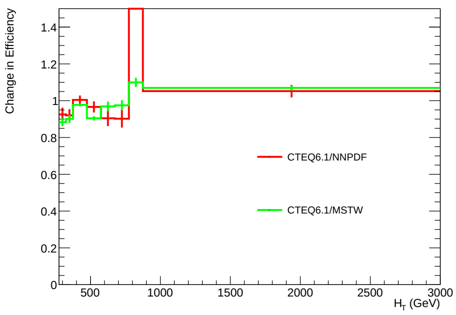

(e) $m_0 = 500\ GeV, m_{1/2} = 500\ GeV$

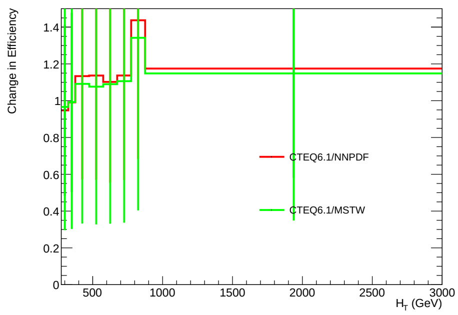

(f) $m_0 = 200\ GeV, m_{1/2} = 1800\ GeV$

Figure 6.18: Figures 6.18(a), 6.18(b) and 6.18(c) show the efficiency per H_T bin for the inclusive selection. The three coloured lines represent the analysis efficiency for a choice of PDF set, the error bars are the RMS of the change in efficiency per PDF set from varying the internal components by 1σ of their error. Figures 6.18(d), 6.18(e) and 6.18(f) show ratio of the change in efficiency from the default PDF set (CTEQ6.1) for three illustrative points in the $m_0, m_{1/2}$ plane of the CMSSM. The change in efficiency in the high efficiency bins is on the order of 10% for all points.

Chapter 7

Conclusion

Bibliography

[1] Updated measurements of the inclusive w and z cross sections at 7 tev. (CMS-AN-10-264), 2010.

[2] Search for supersymmetry with the α_t variable in the 7 tev dataset of 2011. (CMS-AN-11-517), 2011.

[3] Search for supersymmetry in final states with missing transverse energy and 0, 1, 2, 3, or at least 4 b-quark jets in 8 tev pp collisions using the variable alphat. (CMS-PAS-SUS-12-028), 2012.

[4] T Åkesson. The ATLAS experiment at the CERN Large Hadron Collider - CERN Document Server. *Particles*, 1999.

[5] B Alessandro, F Antinori, J Belikov, and C Blume. ALICE: Physics performance report, volume II. *Journal of Physics G: Nuclear and Particle Phyiscs*, January 2006.

[6] Michael Benedikt, Paul Collier, V Mertens, John Poole, and Karlheinz Schindl. *LHC Design Report*. CERN, Geneva, 2004.

[7] Z Bern, G Diana, L J Dixon, F Febres Cordero, S Hoche, and others. Driving Missing Data at Next-to-Leading Order. *arXiv*, D84:114002, 2011.

[8] Michiel Botje, Jon Butterworth, Amanda Cooper-Sarkar, Albert de Roeck, Joel Feltesse, Stefano Forte, Alexander Glazov, Joey Huston, Ronan McNulty, Torbjorn Sjostrand, and Robert Thorne. The PDF4LHC Working Group Interim Recommendations. *arXiv.org*, hep-ph, January 2011.

[9] M Cacciari, G Salam, and G Soyez. The anti-kt jet clustering algorithm. *Journal of High Energy . . .*, January 2008.

[10] Serguei Chatrchyan and others. Determination of Jet Energy Calibration and Transverse Momentum Resolution in CMS. *arXiv*, 6:P11002, 2011.

[11] CMS Collaboration. The Trigger and Data Acquisition Project Technical Design Report, Volume 1, The Level-1 Trigger. *CERN/LHCC 2000-038, CMS TDR 6.1*, 2000.

[12] CMS Collaboration. Data-Driven Estimation of the Invisible Z Background to the SUSY MET Plus Jets Search. Technical report, 2008.

[13] CMS Collaboration. SUSY searches with dijet events. Technical report, 2008.

[14] CMS Collaboration. Search strategy for exclusive multi-jet events from supersymmetry at CMS. Technical report, 2009.

[15] CMS Collaboration. Electron reconstruction and identification at $\sqrt{s} = 7$ TeV. Technical report, 2010.

[16] CMS Collaboration. Isolated Photon Reconstruction and Identification at $\sqrt{s} = 7$ TeV. Technical report, 2010.

[17] CMS Collaboration. Performance of muon identification in pp collisions at $\sqrt{s} = 7$ TeV. Technical report, 2010.

[18] The CMS Collaboration. CMS - The Compact Muon Solenoid. January 1996.

[19] J Marrouche and others. Commissioning the CMS Global Calorimeter Trigger. *CMS IN*, 2010/029, 2010.

[20] J Rademacker. LHCb: Status and Physics Prospects. *Arxiv preprint hep-ex*, January 2005.

[21] Lisa Randall and David Tucker-Smith. Dijet Searches for Supersymmetry at the LHC. *arXiv*, hep-ph, January 2008.

[22] Daniel Stump, Joey Huston, Jon Pumplin, Wu-Ki Tung, H.L. Lai, et al. Inclusive jet production, parton distributions, and the search for new physics. *JHEP*, 0310:046, 2003.

[23] R.S. Thorne, A.D. Martin, W.J. Stirling, and G. Watt. Status of MRST/MSTW PDF sets. 2009.

[24] Maria Ubiali, Richard D. Ball, Luigi Del Debbio, Stefano Forte, Alberto Guffanti, et al. Combined PDF and strong coupling uncertainties at the LHC with NNPDF2.0. 2010.

[25] C Wulz. The CMS experiment at CERN. *cdsweb.cern.ch.*

1 Additional information on triggers

Table 1: List of HT triggers used.

H_T bin (GeV)	Trigger
$275 < H_\mathrm{T} < 325$	HLT_HT250_v*
$325 < H_\mathrm{T} < 375$	HLT_HT300_v*
$375 < H_\mathrm{T} < 475$	HLT_HT350_v*
$H_\mathrm{T} > 475$	HLT_HT400_v*

Table 2: List of α_T triggers used.

$275 < H_\mathrm{T} < 325 GeV$	$325 < H_\mathrm{T} < 375 GeV$
HLT_HT250_AlphaT0p53_v*	HLT_HT300_AlphaT0p52_v*
HLT_HT250_AlphaT0p55_v*	HLT_HT300_AlphaT0p53_v*
HLT_HT250_AlphaT0p58_v*	HLT_HT300_AlphaT0p54_v*
HLT_HT250_AlphaT0p60_v*	HLT_HT300_AlphaT0p55_v*
$375 < H_\mathrm{T} < 475 GeV$	$H_\mathrm{T} > 475 GeV$
HLT_HT350_AlphaT0p51_v*	HLT_HT400_AlphaT0p51_v*
HLT_HT350_AlphaT0p52_v*	HLT_HT400_AlphaT0p52_v*
HLT_HT350_AlphaT0p52_v*	
HLT_HT350_AlphaT0p53_v*	

Table 3: List of Mu_HT triggers used.

$H_\mathrm{T} > 275 GeV$	$H_\mathrm{T} > 375 GeV$
HLT_Mu5_HT200_v*	HLT_Mu5_HT200_v*
HLT_Mu8_HT200_v*	HLT_Mu8_HT200_v*
HLT_Mu15_HT200_v*	HLT_Mu15_HT200_v*
HLT_Mu30_HT200_v*	HLT_Mu30_HT200_v*
HLT_Mu40_HT200_v*	HLT_Mu40_HT200_v*
	HLT_Mu40_HT300_v*

Table 4: List of Photon triggers used.

$H_{\mathrm{T}} > 375GeV$
HLT_Photon75_CaloIdVL_v*
HLT_Photon75_CaloIdVL_IsoL_v*
HLT_Photon90_CaloIdVL_v*
HLT_Photon90_CaloIdVL_IsoL_v*
HLT_Photon125_v*
HLT_Photon135_v*

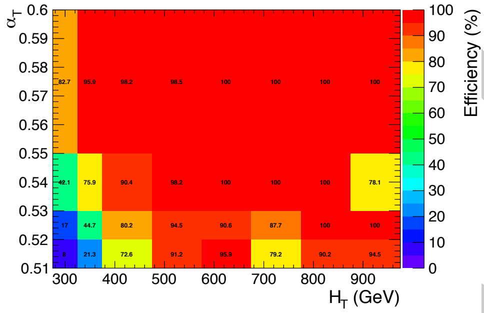

(a) Efficiency (%)

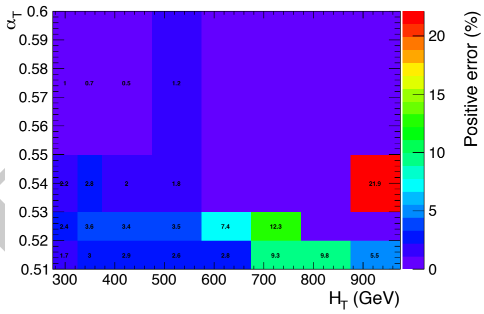

(b) Positive error (%)

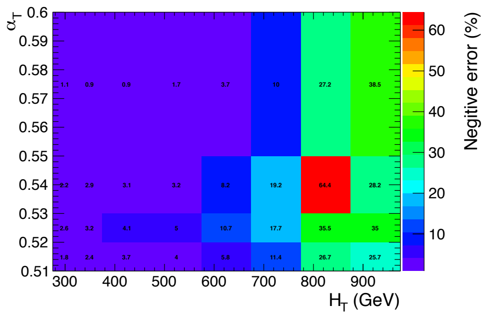

(c) Negative error (%)

Figure 1: Efficiency and associated errors of the α_T trigger in offline bins of H_{T} and α_T.

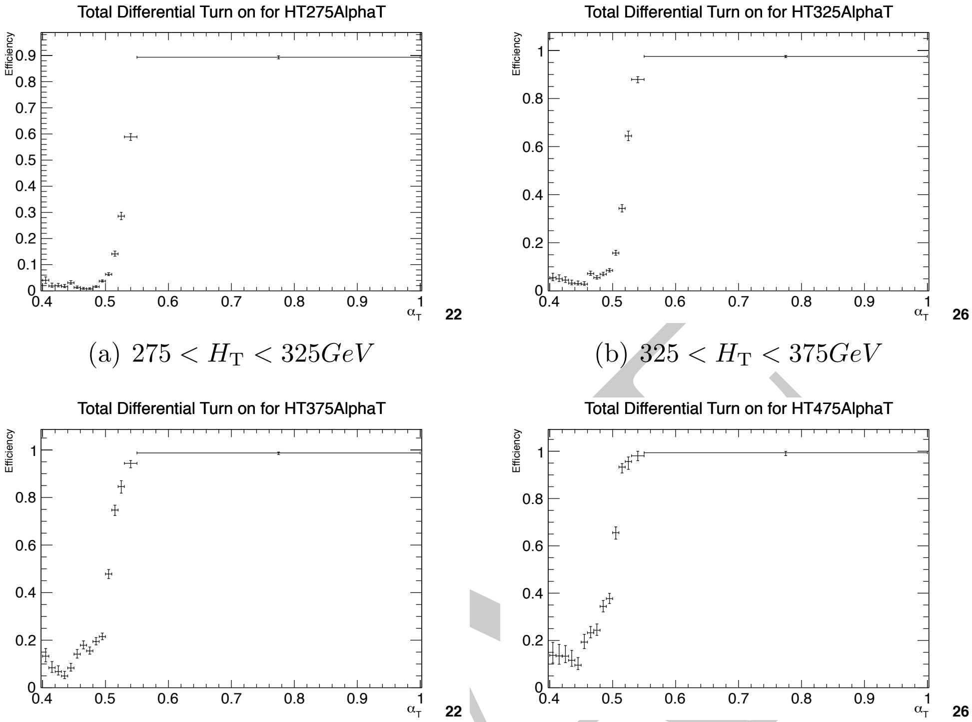

(a) $275 < H_{\mathrm{T}} < 325GeV$

(b) $325 < H_{\mathrm{T}} < 375GeV$

(c) $375 < H_{\mathrm{T}} < 475GeV$

(d) $H_{\mathrm{T}} > 475GeV$

Figure 2: Efficiency turn-on curves for the α_T triggers used to collect events for four different HT regions.

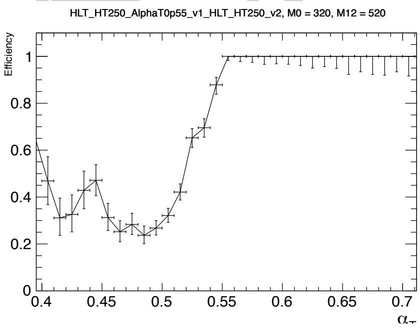

Figure 3: Efficiency turn-on curve for the representative model RM1, with $m_0 = 320GeV$ and $m_{1/2} = 520GeV$, using the α_T trigger with thresholds $H_{\mathrm{T}} > 250GeV$ and $\alpha_T > 0.55$ and an offline signal region defined by $H_{\mathrm{T}} > 275GeV$ and $\alpha_T > 0.55$.

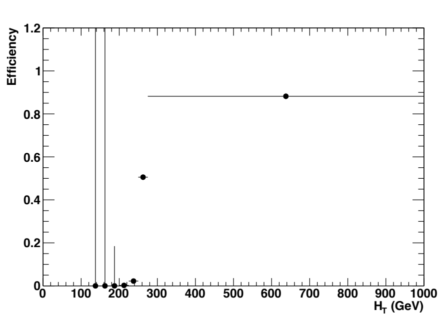

(a) $275 < H_{\mathrm{T}} < 325 GeV$

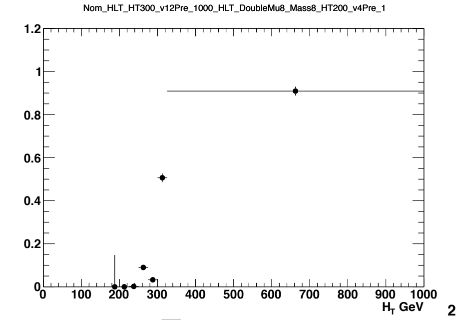

(b) $325 < H_{\mathrm{T}} < 375 GeV$

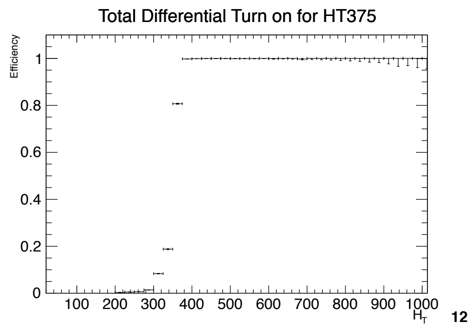

(c) $375 < H_{\mathrm{T}} < 475 GeV$

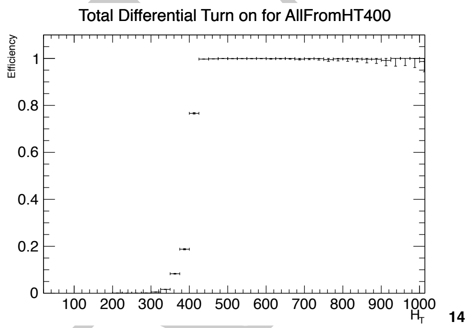

(d) $H_{\mathrm{T}} > 475 GeV$

Figure 4: Efficiency turn-on curves for the H_{T} triggers used to collect events for four different HT regions.

2 Addition information on background estimation methods

2.1 Determination of k_{QCD}

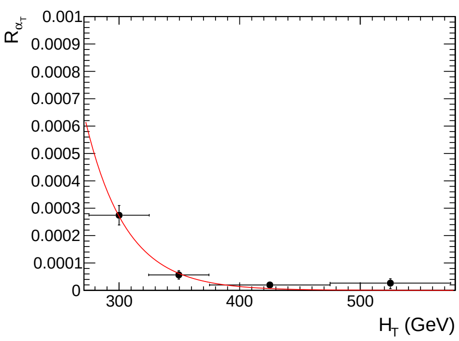

(a) Side-band region B.

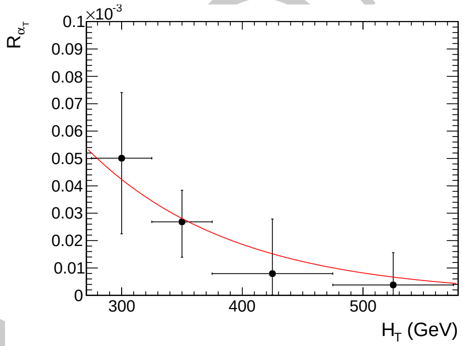

(b) Side-band region C_1.

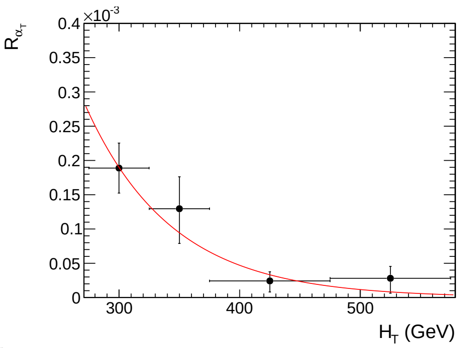

(c) Side-band region C_2.

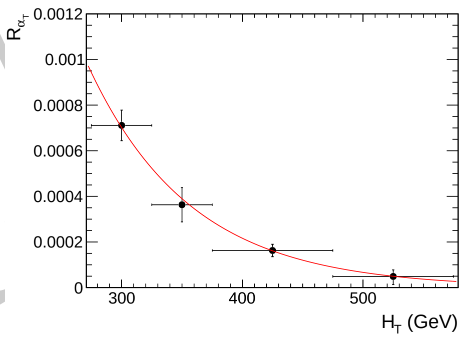

(d) Side-band region C_3.

Figure 5: $R_{\alpha_T}(H_\mathrm{T})$ and exponential fit for various data side-bands. Linear y-axis scale.

3 Closure tests and systematic uncertainties

3.1 Defining muon samples without an α_T requirement

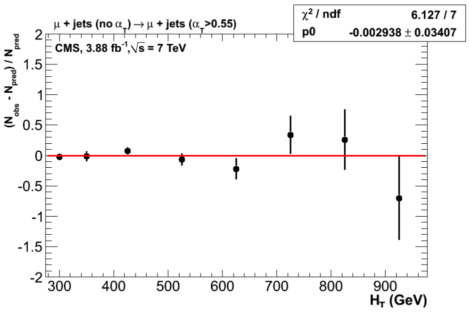

(a) μ + jets sample.

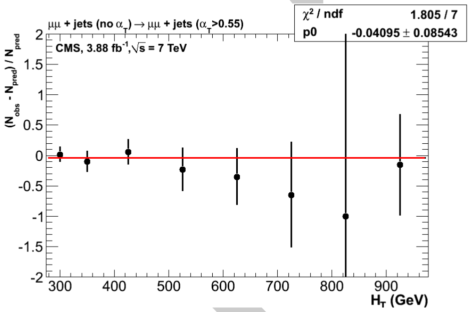

(b) $\mu\mu$ + jets sample.

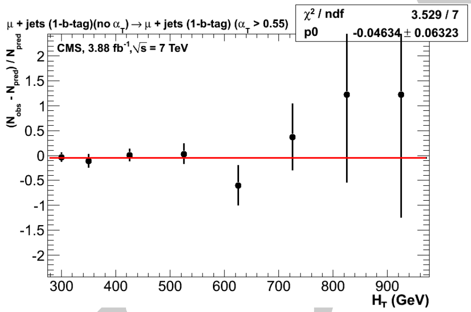

(c) μ + jets sample with 1 b-tag.

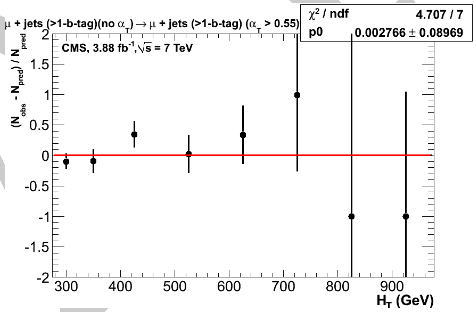

(d) μ + jets sample with >1 b-tags.

Figure 6: Closure tests that demonstrate the MC modelling of the α_T acceptance. The closure tests are performed for both the inclusive analysis with (a) the μ + jets sample and (b) the $\mu\mu$ + jets control sample. Similar tests are performed for the b-tag analysis using (a) the μ + jets sample and a requirement of exactly one b-tag, and (b) the μ + jets sample and a requirement of at least two b-tags. The red lines indicate the constant best fit value across all H_T bins.

3.2 Closure tests for inclusive analysis

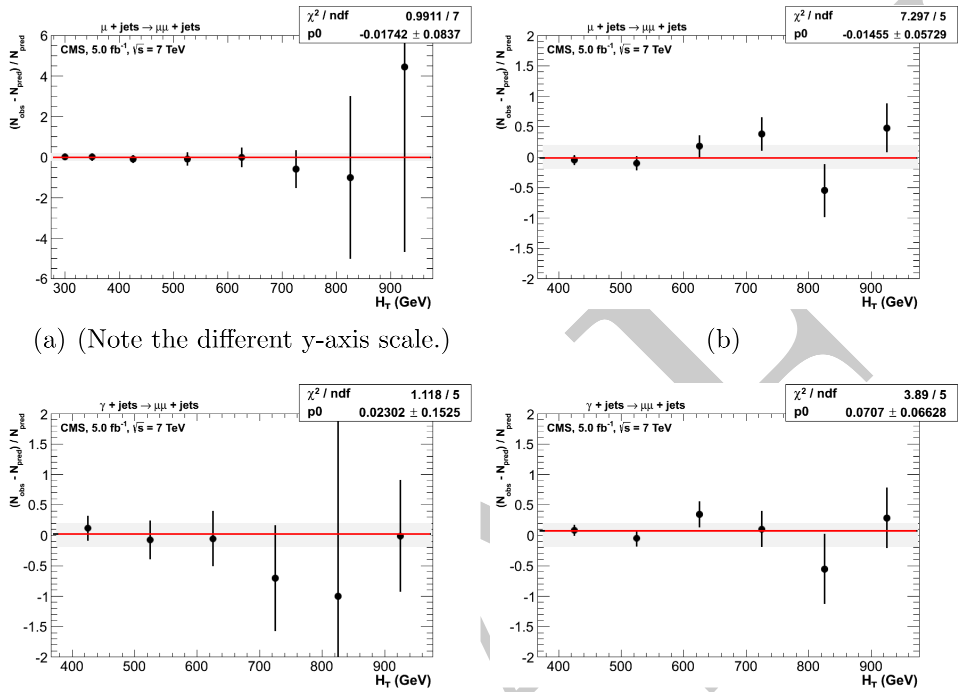

(a) (Note the different y-axis scale.)

(b)

(c)

(d)

Figure 7: Closure tests using yields from one control to predict yields in another sample. The two plots on the left show closure tests which use “low stats” muon samples recorded with the `HT_AlphaT` triggers and defined by offline selection criteria that include an α_T requirement: (a) μ + jets sample $\rightarrow \mu\mu$ + jets sample and (c) γ + jets sample $\rightarrow \mu\mu$ + jets sample. Similarly, the plots on the right show the same closure tests but using “high-stats” muon samples recorded with `Mu_HT` triggers and defined with no offline α_T requirement. The same tests are performed: (b) μ + jets sample $\rightarrow \mu\mu$ + jets sample and (d) γ + jets sample $\rightarrow \mu\mu$ + jets sample. These closure tests are only possible for the six highest H_{T} bins due to the trigger conditions. The red lines indicate the constant best fit value across all H_{T} bins.

3.3 Closure tests for b-tag analysis

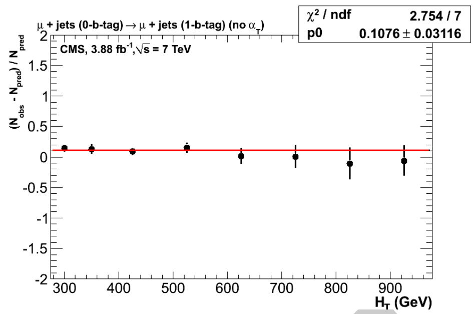

(a) 0 b-tags predicting 1 b-tag.

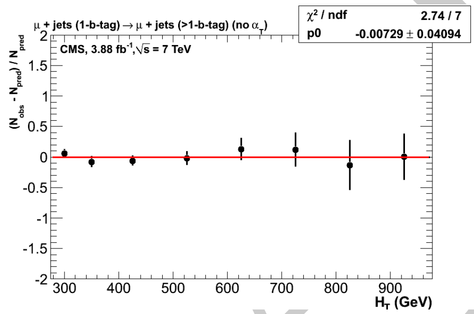

(b) 1 b-tag predicting >1 b-tags.

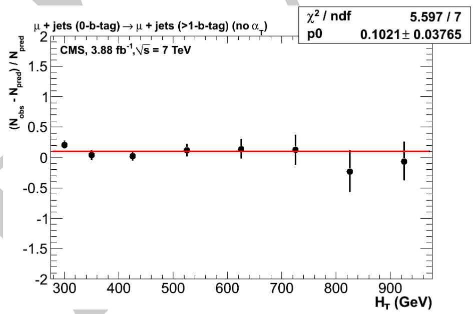

(c) 0 b-tags predicting >1 b-tags.

Figure 8: Closure tests with the μ + jets sample that demonstrate the MC modelling of the b-tagging algorithm and of different sample compositions by for different b-tag multiplicities: (a) 0 b-tags $\to$ 1 b-tag, (b) 1 b-tags $\to$ $\geq$2 b-tags, (c) 0 b-tags $\to$ $\geq$2 b-tags.

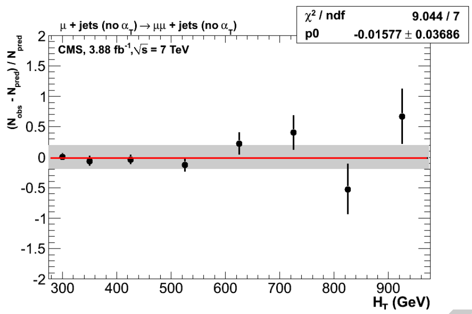

(a) 0 b-tags.

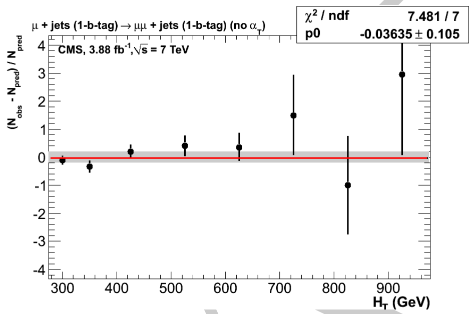

(b) 1 b-tag.

Figure 9: Closure tests using the μ + jets sample to predict the yields in a $\mu\mu$ + jets sample, for events with (a) exactly 0-b-tags and (b) exactly 1-b-tags.

3.4 Closure tests concerning pile-up

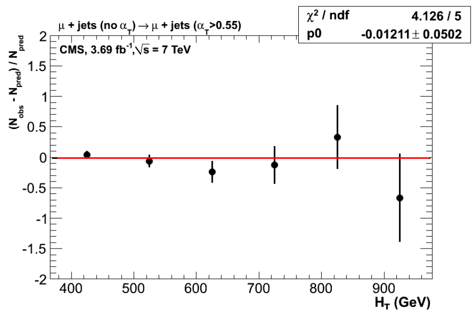

(a)

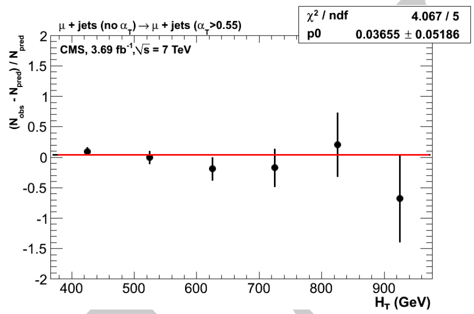

(b)

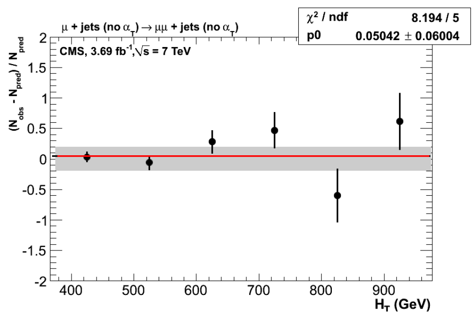

(c)

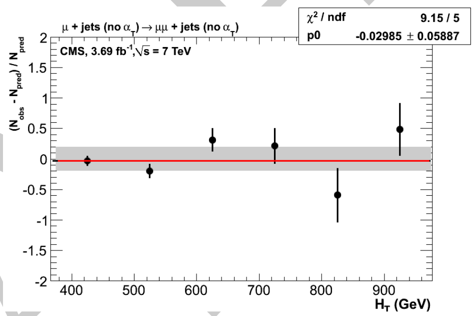

(d)

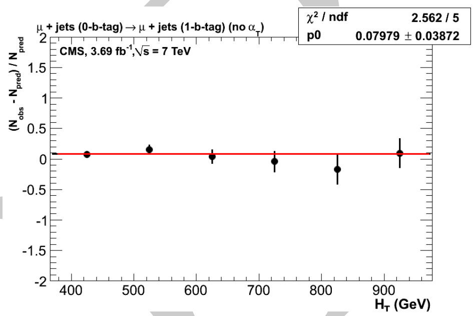

(e)

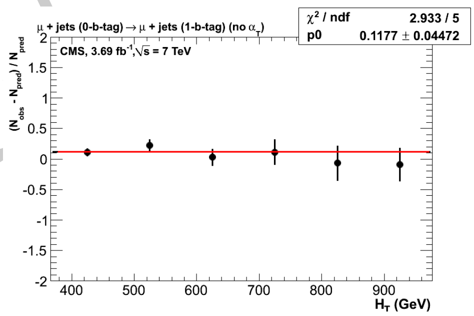

(f)

Figure 10: Closure tests using yields from one control to predict yields in another sample. The three plots on the left show closure tests from the inclusive analysis, which uses jets that are not corrected for the effects of pile-up. On the right, the jets in the analysis *are* corrected for pile-up effects by applying the `L1Offset` jet energy correction. The three closure tests are: probing the MC modelling of the α_T acceptance with the μ + jets sample (a) without and (b) with `L1Offset` jet energy corrections; using the μ + jets sample to predict yields in the $\mu\mu$ + jets sample (a) without and (b) with `L1Offset` jet energy corrections; and using a 0 b-tagged μ + jets sample to predict yields in a 1 b-tagged μ + jets sample (a) without and (b) with `L1Offset` jet energy corrections. The red lines indicate the constant best fit value across all H_{T} bins.

4 Signal efficiency

4.1 CMSSM

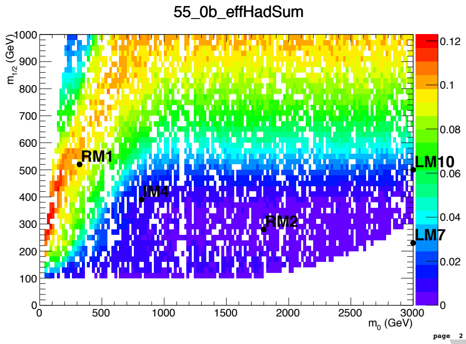

(a) $N_{\mathrm{b-tag}} = 0$.

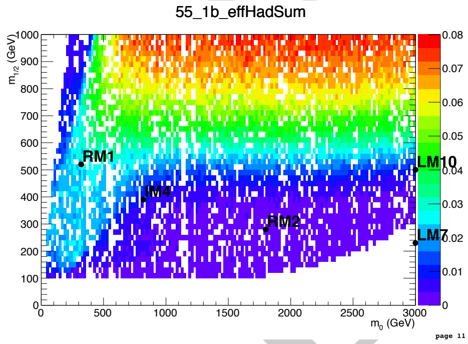

(b) $N_{\mathrm{b-tag}} = 1$.

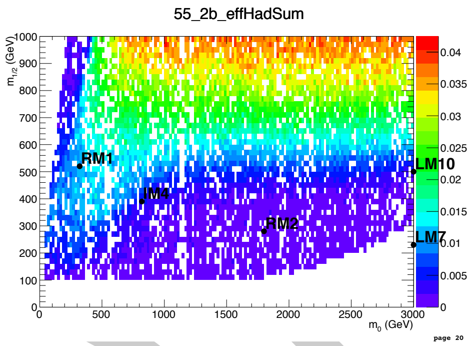

(c) $N_{\mathrm{b-tag}} = 2$.

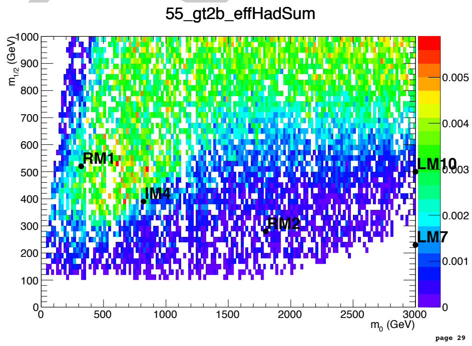

(d) $N_{\mathrm{b-tag}} \geq 3$.

Figure 11: Signal efficiency in the $(m_0, m_{1/2})$ plane of the CMSSM, of the full hadronic signal selection, integrating over all eight H_{T} bins and requiring (a) exactly zero, (b) exactly one, (c) exactly two, and (d) at least three b-tags per event.

4.2 T1

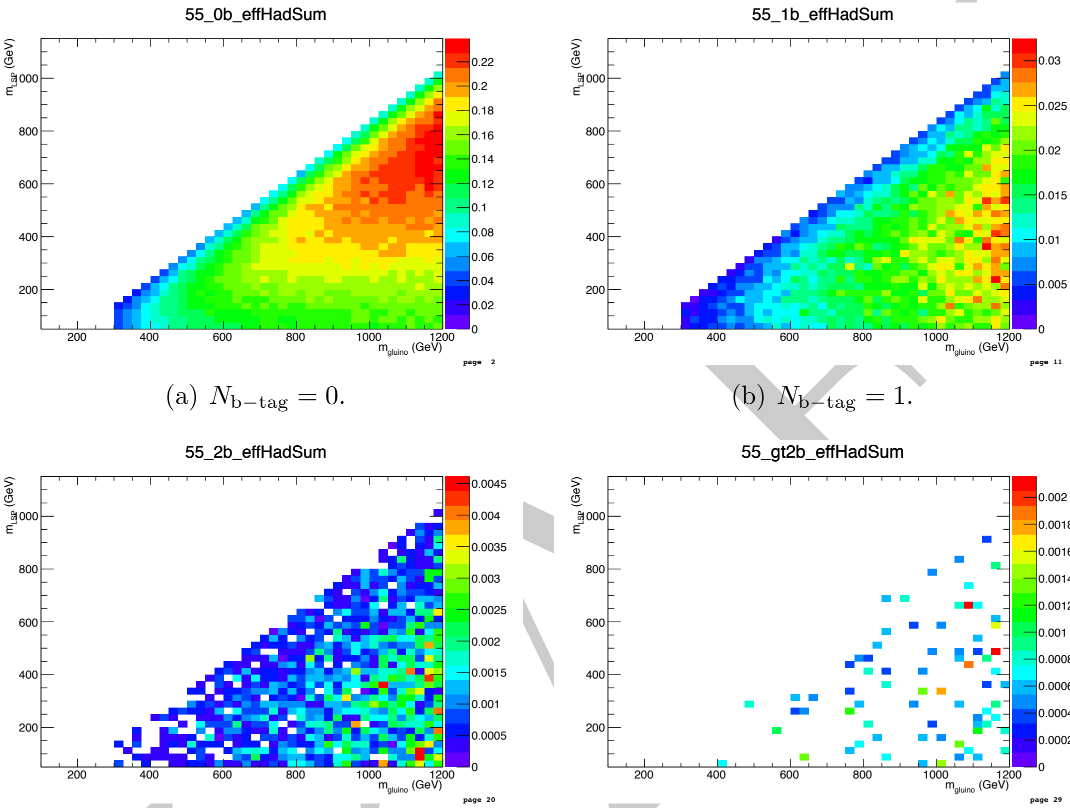

(a) $N_{\mathrm{b-tag}} = 0$.

(b) $N_{\mathrm{b-tag}} = 1$.

(c) $N_{\mathrm{b-tag}} = 2$.

(d) $N_{\mathrm{b-tag}} \geq 3$.

Figure 12: Signal efficiency in the $(m_{\mathrm{gl}}, m_{\mathrm{LSP}})$ plane of the `T1` simplified model, of the full hadronic signal selection, integrating over all eight H_{T} bins and requiring (a) exactly zero, (b) exactly one, (c) exactly two, and (d) at least three b-tags per event.

4.3 T2

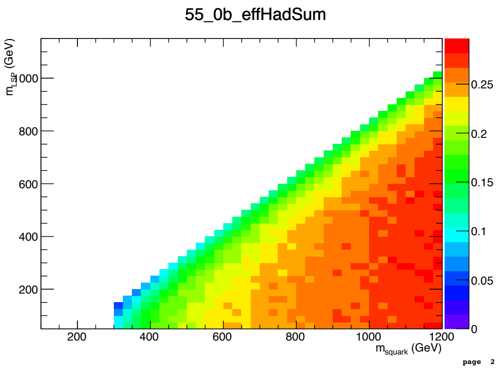

(a) $N_{\mathrm{b-tag}} = 0$.

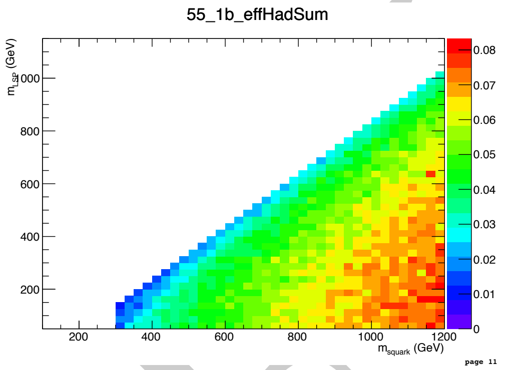

(b) $N_{\mathrm{b-tag}} = 1$.

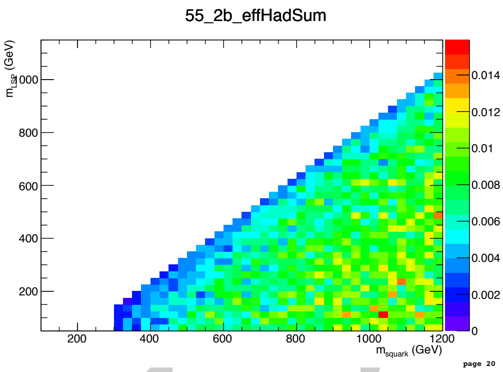

(c) $N_{\mathrm{b-tag}} = 2$.

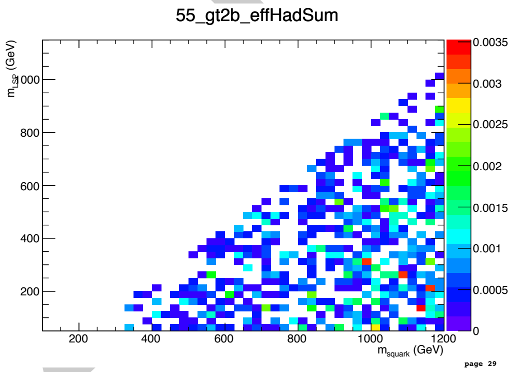

(d) $N_{\mathrm{b-tag}} \geq 3$.

Figure 13: Signal efficiency in the $(m_{\mathrm{sq}}, m_{\mathrm{LSP}})$ plane of the T2 simplified model, of the full hadronic signal selection, integrating over all eight H_{T} bins and requiring (a) exactly zero, (b) exactly one, (c) exactly two, and (d) at least three b-tags per event.

4.4 T2tt

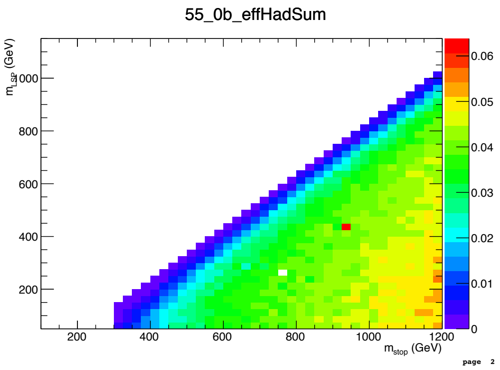

(a) $N_{\rm b-tag} = 0$.

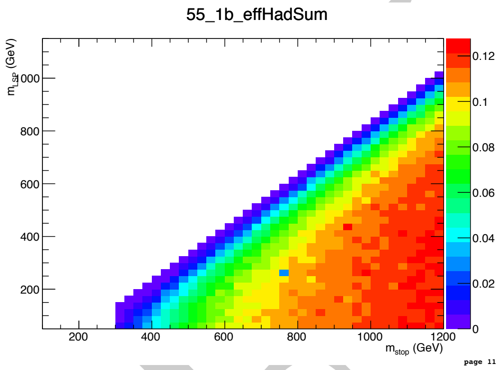

(b) $N_{\rm b-tag} = 1$.

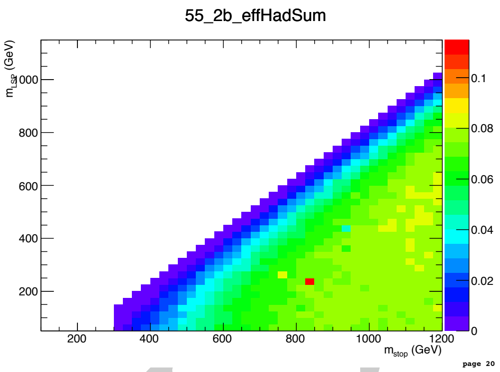

(c) $N_{\rm b-tag} = 2$.

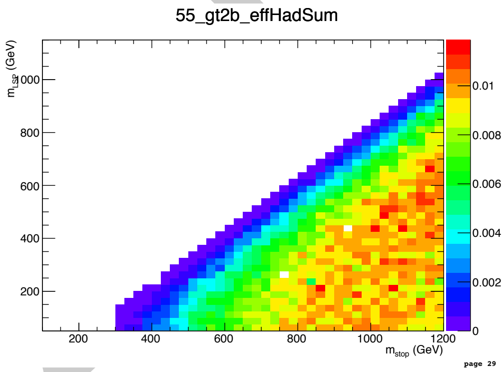

(d) $N_{\rm b-tag} \geq 3$.

Figure 14: Signal efficiency in the $(m_{\rm sq}, m_{\rm LSP})$ plane of the `T2tt` simplified model, of the full hadronic signal selection, integrating over all eight $H_{\rm T}$ bins and requiring (a) exactly zero, (b) exactly one, (c) exactly two, and (d) at least three b-tags per event.

4.5 T2bb

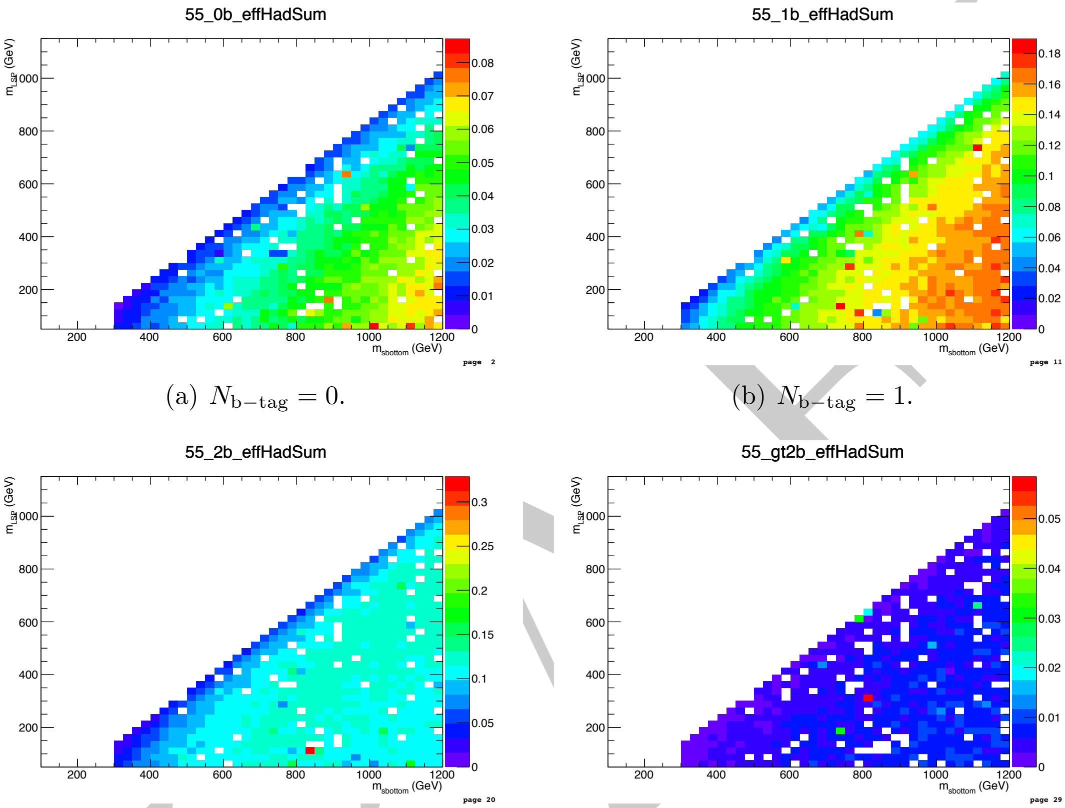

(a) $N_{\mathrm{b-tag}} = 0$. (b) $N_{\mathrm{b-tag}} = 1$.

(c) $N_{\mathrm{b-tag}} = 2$. (d) $N_{\mathrm{b-tag}} \geq 3$.

Figure 15: Signal efficiency in the $(m_{\mathrm{sq}}, m_{\mathrm{LSP}})$ plane of the `T2bb` simplified model, of the full hadronic signal selection, integrating over all eight H_{T} bins and requiring (a) exactly zero, (b) exactly one, (c) exactly two, and (d) at least three b-tags per event.

1 ## 4.6 T1tttt

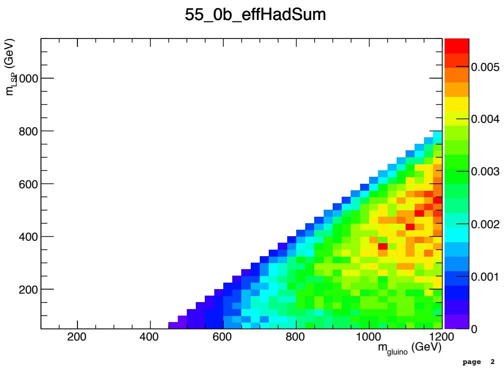

(a) $N_{\mathrm{b-tag}} = 0$.

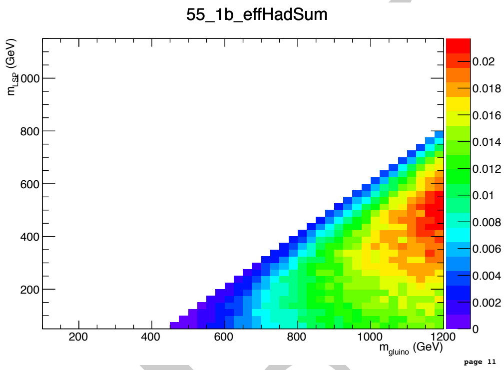

(b) $N_{\mathrm{b-tag}} = 1$.

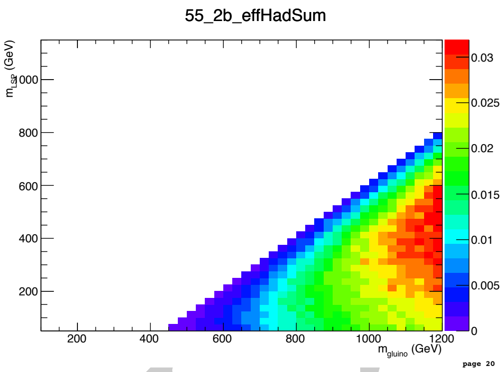

(c) $N_{\mathrm{b-tag}} = 2$.

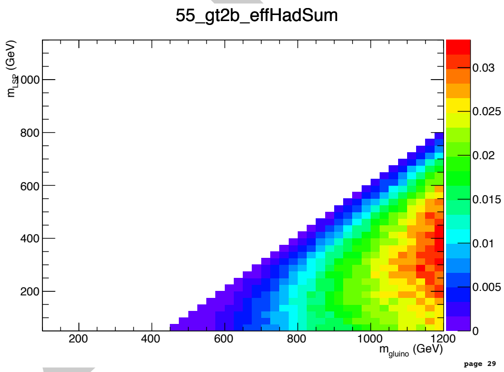

(d) $N_{\mathrm{b-tag}} \geq 3$.

Figure 16: Signal efficiency in the $(m_{\mathrm{gl}}, m_{\mathrm{LSP}})$ plane of the `T1tttt` simplified model, of the full hadronic signal selection, integrating over all eight H_{T} bins and requiring (a) exactly zero, (b) exactly one, (c) exactly two, and (d) at least three b-tags per event.

4.7 T1bbbb

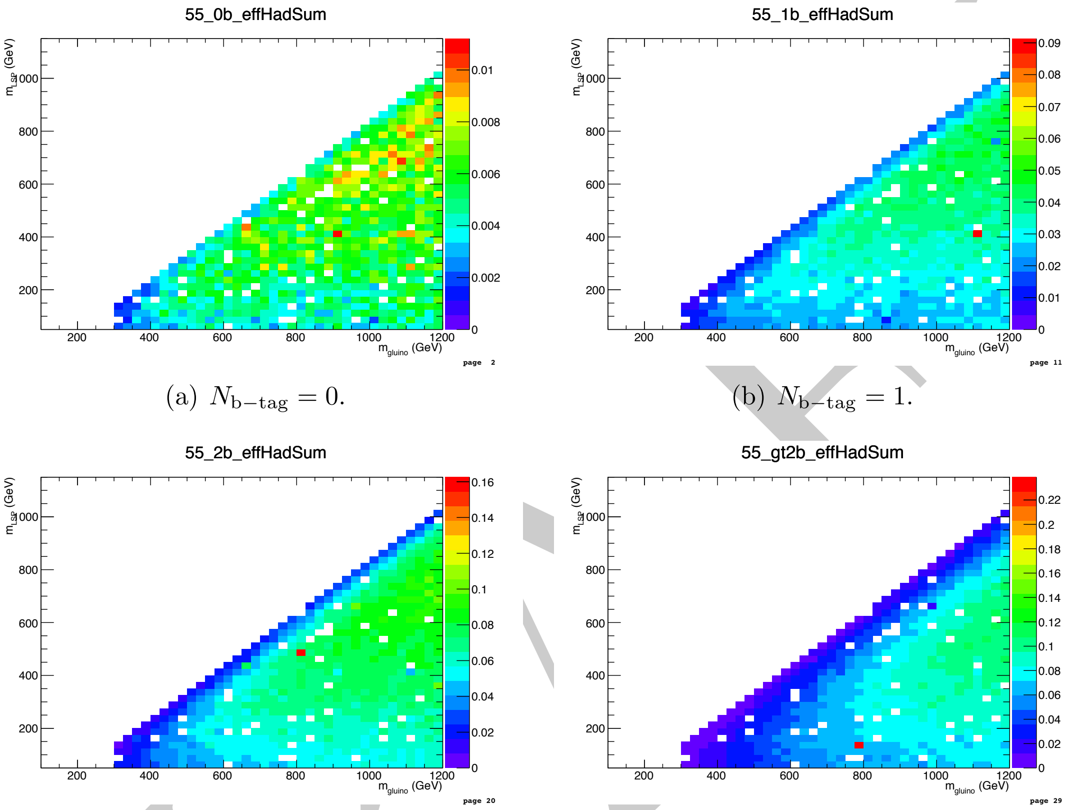

(a) $N_{\mathrm{b-tag}} = 0$.

(b) $N_{\mathrm{b-tag}} = 1$.

(c) $N_{\mathrm{b-tag}} = 2$.

(d) $N_{\mathrm{b-tag}} \geq 3$.

Figure 17: Signal efficiency in the $(m_{\mathrm{gl}}, m_{\mathrm{LSP}})$ plane of the `T1bbbb` simplified model, of the full hadronic signal selection, integrating over all eight H_{T} bins and requiring (a) exactly zero, (b) exactly one, (c) exactly two, and (d) at least three b-tags per event.

4.8 Signal contamination for `T1tttt`

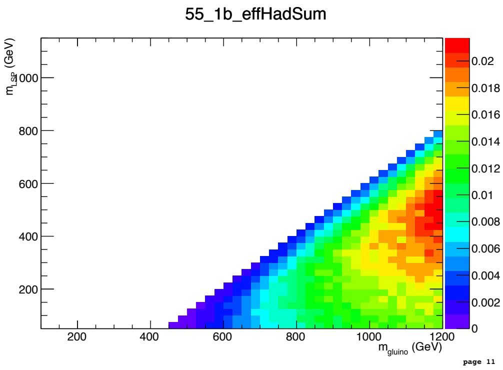

(a) Hadronic signal region, $N_{\mathrm{b-tag}} = 1$

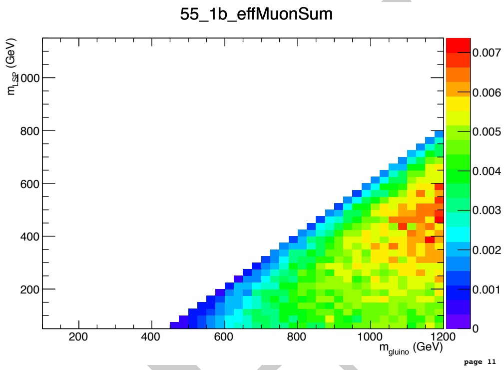

(b) Muon control sample, $N_{\mathrm{b-tag}} = 1$

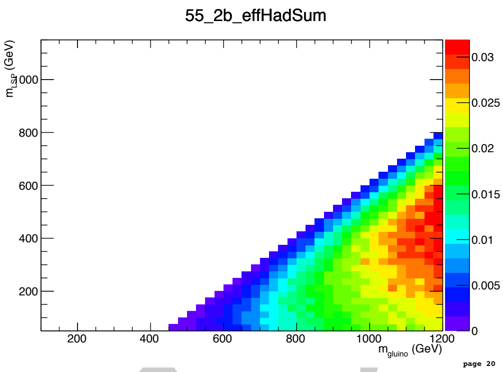

(c) Hadronic signal region, $N_{\mathrm{b-tag}} = 2$

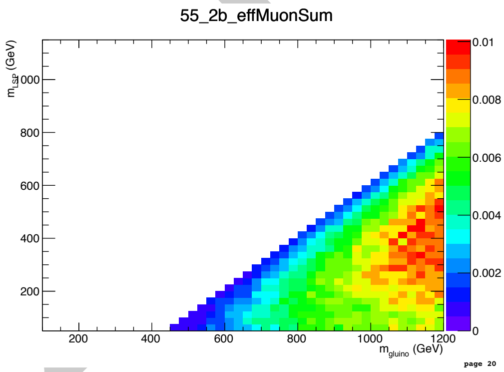

(d) Muon control sample, $N_{\mathrm{b-tag}} = 2$

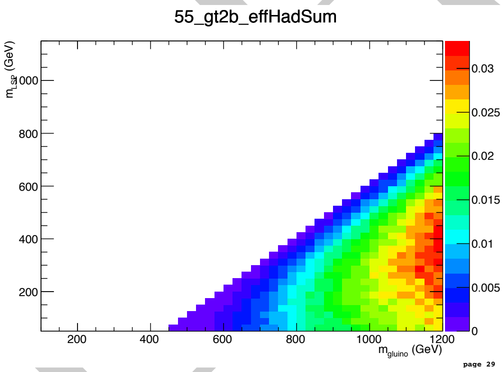

(e) Hadronic signal region, $N_{\mathrm{b-tag}} \geq 3$

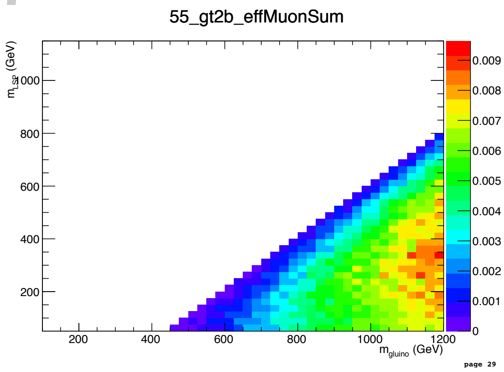

(f) Muon control sample, $N_{\mathrm{b-tag}} \geq 3$

Figure 18: Signal efficiency in the planes of simplified model `T1tttt`, of the (left) hadronic signal sample selection or (right) single muon control sample selection, integrating over all eight H_{T} bins and requiring (top) exactly one, (middle) exactly two, or (bottom) at least three b-tags per event.